Cross sections for single-electron capture from heliumlike targets by fast heavy nuclei

Nenad Milojević,[1] Ivan Mančev,[1] Danilo Delibašić,[1] and Dževad Belkić[2,3]
[1]*Department of Physics, Faculty of Sciences and Mathematics, University of Niš, P.O. Box 224, 18000 Niš, Serbia*
[2]*Karolinska Institute, Department of Oncology-Pathology, P.O. Box 260, SE-171 76, Stockholm, Sweden*
[3]*Radiation Physics and Nuclear Medicine, Karolinska University Hospital, SE-171 76, Stockholm, Sweden*

(Received 23 June 2022; revised 6 March 2023; accepted 2 May 2023; published 17 May 2023)

Single charge-exchange in collisions of heavy bare nuclei with the ground state of two-electron atomic targets is described perturbatively as a four-body problem. The employed four-body boundary-corrected continuum intermediate state (BCIS-4B) method considers the correlated and uncorrelated target wave functions φ_i. A thorough examination is performed for the formation of any final hydrogen-like nlm state of the captured electron. For arbitrary projectile and target nuclear charges, the nine-dimensional integral in the transition amplitude is reduced to a two-dimensional numerical quadrature. The general analysis is applied to one-electron capture by protons from helium targets beginning with the lower edge (10 keV) of intermediate energies and extending to the higher (12.5 MeV) domain. These include the main peaks (Massey, Thomas) due to single and double scattering, respectively. The results encompass over 70 state-selective and state-summed cross sections ($n \leqslant 6$, $0 \leqslant l \leqslant n-1$, $-l \leqslant m \leqslant l$). In comparison to measurements, the electronic correlations in φ_i greatly improve the overall performance of the BCIS-4B method around the Massey peak, below about 100 keV. Moreover, while largely outperforming the three-body boundary-corrected continuum intermediate state method, the cross sections in the BCIS-4B with the correlated φ_i compare excellently overall with the available experimental data at 10 to 12 500 keV. Hence, the BCIS-4B method, with its built-in two main capture mechanisms (one-step Massey and two-step Thomas) is capable of spanning impact energies covering three or more orders of magnitude at which the state-summed cross sections vary over 11 orders of magnitude.

DOI: 10.1103/PhysRevA.107.052806

I. INTRODUCTION

Charge-exchange in collisions of heavy nuclei with atomic targets has been the subject of intense experimental and theoretical studies over the years. Developments in this problem area were driven by two main reasons. One is the fundamental importance of interactive dynamics in collisions involving particle rearrangements. The other is in cross-disciplinary applications ranging from astrophysics [1,2] and plasma physics [3–6] through thermonuclear fusion [3–8] to ion transport physics in radiotherapy for medicine [9–21]. On the theoretical side, explored in detail were both the perturbative (Born-type, distorted-wave-type) methods [22–29] and the nonperturbative [atomic expansions (AE), close coupling (CC)] methods [30–37].

The present study is within the quantum-mechanical perturbative distorted wave formalism for one-electron capture by heavy nuclei of charge Z_P from two-electron atomic targets $(Z_T; e_1, e_2)_{1s^2}$ of nuclear charge Z_T. This process is symbolized as $Z_P + (Z_T; e_1, e_2)_{1s^2} \to (Z_P, e_1)_{nlm} + (Z_T, e_2)_{1s}$, where the captured electron is taken to be in an arbitrary nlm state $(Z_P, e_1)_{nlm}$ while, as an example, the target remainder $(Z_T, e_2)_{1s}$ is left in its ground state $(1s)$. The four-body boundary-corrected continuum intermediate state (BCIS-4B) method is extended to this general process. An earlier application of this method dealt only with the ground state $(nlm = 1s)$ of the transferred electron [38]. All four particles were treated as active participants to every considered transition $(1s^2 \to nlm)$. The BCIS-4B method satisfies the correct boundary conditions in both the entrance and exit channels, following the prescriptions of the Coulomb scattering theory [22–26,39–41].

Often, single charge-exchange in the original $Z_P + (Z_T; e_1, e_2)_{1s^2}$ four-body collisions has been described in an effective one-electron framework, where the noncaptured electron e_2 is taken as passive from the onset. As such, the only trace of e_2 in the ensuing effective model is in a partial shielding of the bare nuclear charge Z_T. In other words, the modeled target nucleus acquires a screened charge $Z_T^{\rm eff} < Z_T$ on account of the presence of e_2. In this formalism, the target active electron e_1 experiences an effective potential $V_T^{\rm eff}$ generated by Z_T and the passive electron e_2. As an approximation of the Roothan-Hartree-Fock (RHF) interaction $V_T^{\rm RHF}$, the potential $V_T^{\rm eff}$ has usually been chosen to be purely Coulombic [42], static or their sum [32], and so on.

Due to the complete disappearance of e_2, the effective one-electron problem becomes amenable to descriptions by purely three-body methods. In this setting, different one-electron target wave functions were used (hydrogen-like, RHF, etc). Even within a Coulombic $V_T^{\rm eff}$, various choices of $Z_T^{\rm eff}$ were made (e.g., the Slater-Hylleraas or the binding-energy screenings (BES), etc. [23]). Examples of such simplified perturbative theories are the three-body versions of the continuum distorted wave (CDW-3B) method [22] and the boundary-corrected continuum intermediate state (BCIS-3B) method [42]. It is of interest to learn about the possible differences between the three- and four-body formalisms. We shall juxtapose the findings from the BCIS-3B and BCIS-4B methods.

In Ref. [42] for the BCIS-3B method, the mentioned one-electron formalism was employed, describing the ground state of a two-electron target by a hydrogen-like wave function with the standard effective or screened Slater-Hylleraas nuclear charge Z_T^{eff}.

The BCIS-4B method in its prior version is a hybrid distorted-wave scattering formalism [25,38]. It coincides with the four-body boundary-corrected first Born (CB1-4B) method [43,44] in the entrance channel. This BCIS-4B method is the same as the associated four-body continuum distorted wave (CDW-4B) method [26,41,45] in the exit channel. Moreover, the perturbation potential V_i in the transition amplitude of the prior BCIS-4B method is identical to that in the prior CB1-4B method. In the entrance channel, the prior BCIS-4B method includes a single Coulomb distortion caused by the relative motion of the two heavy scattering aggregates in the residual field $Z_P(Z_T-2)/R$, which is the asymptotic value of V_i at large internuclear separations R. The exit channel of the BCIS-4B method contains the product of the two distorting factors. One distortion is the electronic full Coulomb wave function for the two point charges $\{e_1, Z_T - 1\}$. The other factor is the Coulomb distortion for the relative motion of heavy particles governed by the asymptotic potential $Z_P(Z_T-1)/R$. Here, Z_T-1 indicates that the bare nuclear charge Z_T is considered as being screened by non-transferred electron e_2 in the target remainder $(Z_T, e_2)_{1s}$. The ionization channel dominates over capture at high energies. Therefore, inclusion of the transient ionization continua can appreciably alter the probability of single charge-exchange.

The underlying physical mechanism in the BCIS-4B method assumes that the active electron is first ionized and then captured from a continuum into the bound nlm state $(Z_P, e_1)_{nlm}$ around the scattered projectile Z_P. It is because of these transient ionizing continuum intermediate states in the exit channel that the prior BCIS-4B method is categorized as a second-order distorted wave theory. The said two-step mechanism secures a perturbative quantum-mechanical description of the classical billiard-type Thomas double scattering [40]. This second-order effect refers to two successive collisions of the active electron e_1, one with the projectile and the other with the target nucleus, $Z_P - e_1 - Z_T$. In differential cross sections, such an effect yields a peak at a critical angle $\theta_c = (1/M_P)\sin 60^\circ$ mrad in the laboratory system, independent of incident velocity v. Here, M_P is the mass of Z_P, so that for protons as projectiles, it follows that $\theta_c = 0.472$ mrad in the laboratory system. At sufficiently high impact energies E, differential cross sections that include the Thomas double scattering dominate over the direct collisional pathway $Z_P - e_1$, which is responsible for the kinematic, velocity-matching capture of e_1. This dominance is not restricted to angular distributions alone. Quite the contrary, unlikely as it may seem at first, the high-energy asymptotes of the total cross sections (for any $s \to s$ transition) that include the two-step collisions fall off more slowly as v^{-11} relative to the v^{-12} decline caused by the one-step collisions [40].

All the previous applications of the BCIS-3B and BCIS-4B methods [25,38,46–48] were concerned only with the ground-to-ground-state capture processes. Recently, the BCIS-3B method was generalized to transitions involving any final nlm state of the transferred electron [42,49,50]. This is a motivation to extend also the BCIS-4B method to one-electron capture into an arbitrary hydrogen-like nlm state by bare multiply charged heavy nuclei from the ground state of helium-like atomic targets. For this collision, the consequences of the two extra effects in the BCIS-4B method are investigated. One is the interelectronic correlation effects in the two-electron target wave functions. The other is an additional channel for the capture of electron e_1 by way of the Coulomb interaction $Z_P - e_2$ between the nontransferred electron e_2 and Z_P. Neither effect is included in the BCIS-3B method [42], which, as stated, replaced the original four-body $Z_P + (Z_T; e_1, e_2)_{1s^2}$ collision with two active electrons by its three-body charge-exchange companion involving explicitly only one electron. In the latter scattering, the noncaptured electron e_2 and the $e_1 - e_2$ correlations are absent altogether.

First, we will succinctly outline the announced update of the BCIS-4B method for the mentioned general charge-exchange problem with the usage of the *two-electron* target wave function of Silverman *et al.* [51] with its 95% radial static correlations. This upgrade is also adaptable to the corresponding *two-electron* uncorrelated wave function of Hylleraas [52]. With both the correlated and uncorrelated target wave functions, a large reduction, by analytical means, is carried out of the starting nine-dimensional integral from the transition amplitude T_{if} for an arbitrary final hydrogen-like nlm state of the captured electron. The outcome of a protracted analysis is a two-dimensional numerical quadrature for T_{if}. This is of notable practical relevance since one of the bottlenecks of a number of the second-order perturbative methods is precisely the occurrence of the Coulomb multi-dimensional integrals in T_{if}. Such a stumbling block is especially exacerbated when both differential $(dQ/d\Omega)_{if}$ and total Q_{if} cross sections contain the Coulomb distorting functions for electronic *and* nuclear motions, as in the BCIS-4B method. The accomplished dimensionality reduction in this theory cannot be overstated since, with exactly the same analytical procedure, the original seven-dimensional integral in T_{if} for the BCIS-3B method for any final hydrogen-like nlm state is also reduced to a two-dimensional quadrature [42]. Customarily, four-body methods are computationally much more demanding than their three-body counterparts. For instance, the transition amplitudes in the CDW-3B and CDW-4B methods for single charge-exchange are given by a completely analytical expression [22] and by a three-dimensional numerical quadrature [45], respectively.

Second, the general result for T_{if} in the BCIS-4B method is used to compute Q_{if} and $(dQ/d\Omega)_{if}$ for the process $H^+ + He(1s^2) \to H(nlm) + He^+(1s)$ in a broad range of intermediate and high energies ($E = 10$–$12\,500$ keV). Some simpler theories, e.g., the CB1 method [or the eikonal approximation (EA) or symmetric-eikonal (SE) approximation, etc.] may give reasonable results for Q_{if}, but only at energies where the two-step mechanism is insignificant. However, with the double scattering neglected in such first-order methods, the Thomas peak is invariably absent from, e.g., $(dQ/d\Omega)_{1s}$ and, moreover, the ensuing total cross section $Q_{1s} \sim v^{-12}$ is at variance with the correct result $Q_{1s} \sim v^{-11}$ ($v \gg 1$ a.u.). It is then important to have a single perturbative theory capable of simultaneously yielding good results for Q_{if} and $(dQ/d\Omega)_{if}$ from the onset of intermediate E (a few tens of keV, around

the Massey peak) up to high energies (tens of MeV, covering the Thomas peak).

The present state-resolved and state-summed cross sections in the BCIS-4B method include over 70 transitions $1s^2 \to nlm$ for $1 \leqslant n \leqslant 6$ with all the degenerate lm sublevels of the captured electron. Cross sections Q_Σ for any nlm are deduced from Q_n (summed over lm) by assuming the n^{-3} population of the excited states H(n). The selections of energies E and the $\{nl, n, \Sigma\}$ states in H(nl, n, Σ) are guided by the availability of the measured cross sections. The corresponding experimental data exist for the formation of H(nl) with $n \leqslant 4$ ($2s$, $2p$, $3s$, $3p$, $3d$, $4s$) and H(n) with $2 \leqslant n \leqslant 6$ as well as for H(Σ) (all n) [32,53–89]. The goal in comparing these experiments with our theoretical results is to determine whether the BCIS-4B method can systematically and reliably describe the measured cross sections. Such comparisons also include the BCIS-3B method for Q_{if} and $(dQ/d\Omega)_{if}$ to assess the anticipated advantages of passing from a three- to a four-body theory.

Additionally, special attention is paid to evaluate the influence of the said two extra effects in the present four-body formalism. As stated, one is a supplementary capture channel, where electron e_1 is transferred to the projectile by the action of electron e_2 through the $Z_P - e_2$ Coulomb potential, included in the perturbation interaction V_i. The other is the $e_1 - e_2$ correlation in the two-electron target wave function of Silverman *et al.* [51] as compared to the associated two-electron uncorrelated Hylleraas orbitals [52].

Atomic units will be used throughout unless otherwise stated.

II. THEORY

We examine single-electron capture in collisions of a fast heavy projectile nucleus P of mass M_P and charge Z_P with a two-electron atomic target, assumed to be in its singlet state ($1s^2\ :\ ^1S$), with its total spin equal to zero. In such a helium-like atomic target, the two electrons are indistinguishable, except for having different spin projections (up and down). This permits two separate calculations of the probabilities for the capture of either electron. Since neither probability depends on spin, the total probability is two times the probability for capture of either electron. The equivalent procedure, using no spin-dependent interactions, allows from the onset to consider the two electrons as distinguishable in the ground singlet state of a helium-like target. In such a setting, e.g., the electron e_1 can be viewed as being captured, while electron e_2 would be in the target single charged ion. The calculated probability shall be the same if electrons e_1 and e_2 were to exchange their roles. Therefore, it suffices to find the probability of only one of these two equivalent pathways and subsequently double the result.

This four-body problem with transfer of e_1 from a target to a projectile is customarily schematized as

$$Z_P + (Z_T; e_1, e_2)_{1s^2:\,^1S} \longrightarrow (Z_P, e_1)_{nlm} + (Z_T, e_2)_{1s}. \quad (1)$$

Here, the parentheses symbolize the bound states and nlm is the triple of the standard quantum numbers of the hydrogen-like system formed by way of the capture of electron e_1 by Z_P. Let $\vec{x}_j$ and $\vec{s}_j$ be the position vectors of e_j relative to $Z_{T,P}$, respectively ($j = 1, 2$). The position vector of Z_P with respect to Z_T is labeled by $\vec{R}$, where $\vec{R} = \vec{x}_1 - \vec{s}_1 = \vec{x}_2 - \vec{s}_2$. Further, in the entrance channel, let $\vec{r}_i$ be the position vector of Z_P relative to the center of mass of $(Z_T; e_1, e_2)_{1s^2}$. Likewise, in the exit channel, let $\vec{r}_f$ be the position vector of the center of mass of $(Z_T, e_2)_{1s}$ with respect to the center of mass of $(Z_P, e_1)_{nlm}$.

The prior form of the transition amplitude in the BCIS-4B method for collision (1) is defined by

$$T_{if} = \langle \chi_f^- | V_i | \Phi_i^+ \rangle, \quad V_i = V_{i,P1} + V_{i,P2},$$
$$V_{i,Pj} = \frac{Z_P}{R} - \frac{Z_P}{s_j} \ (j = 1, 2). \quad (2)$$

Perturbation potential V_i is of short-range at $R \to \infty$ and so are its two components $V_{i,P1}$ and $V_{i,P2}$. In process (1), the direct capture mechanism is by the interaction $V_{i,P1}$ of e_1 with Z_P. Additionally, an indirect capture of e_1 is also possible through an extra channel by the interaction $V_{i,P2}$ of e_2 with Z_P. This indirect capture of e_1 is mediated by the $e_1 - e_2$ correlation in the target. It is then important that the BCIS-4B method uses a highly correlated wave function for target $(Z_T; e_1, e_2)_{1s^2:\,^1S}$. The wave function of Silverman *et al.* [51] with its 95% of all the radial correlations was used in Ref. [38] for process (1) with $nlm = 1s$ and will also be employed in the present work for an arbitrary triple nlm.

With the Coulomb distortions $\mathcal{E}_{i,f}^{\pm} = e^{\pm i\nu_{i,f} \ln(vR \mp \vec{v}\cdot\vec{R})}$, the channel states are $\Phi_i^+ = \varphi_i(\vec{x}_1, \vec{x}_2) e^{i\vec{k}_i\cdot\vec{r}_i} \mathcal{E}_i^+$ and

$$\chi_f^- = \frac{N^-(\nu_T)}{\sqrt{2}} e^{-i\vec{k}_f\cdot\vec{r}_f} \mathcal{E}_f^- [\varphi_{nlm}(\vec{s}_1)\varphi_{1s}(\vec{x}_2)$$
$$\times\ {}_1F_1(-i\nu_T, 1, -ivx_1 - i\vec{v}\cdot\vec{x}_1) + \mathrm{exc}(1,2)], \quad (3)$$

where exc(1, 2) symbolizes repetition of the preceding term in the square brackets by interchanging the role of two electrons. Here, $\nu_i = Z_P(Z_T - 2)/v$, $\nu_f = Z_P(Z_T - 1)/v$, $\nu_T = (Z_T - 1)/v$, and $N^-(\nu_T) = e^{\pi\nu_T/2}\Gamma(1 + i\nu_T)$. The velocity vector $\vec{v}$ of projectile P is along the Z axis ($\vec{v} = v\hat{\vec{Z}}$). The function $N^-(\nu_T)\,{}_1F_1(-i\nu_T, 1, -ivx_1 - i\vec{v}\cdot\vec{x}_1)$ in χ_f^- is a part of the electronic full continuum Coulomb wave function for the attractive potential $-(Z_T - 1)/x_1$. The quantity $Z_T - 1$ is the charge of the screened target core $(Z_T, e_2)_{1s}$. The symbol Γ denotes the gamma function and ${}_1F_1(a, b, z)$ is the confluent hypergeometric function. Furthermore, $\vec{k}_i$ and $\vec{k}_f$ are the initial and final wave vectors, respectively. Wave function $\varphi_i(\vec{x}_1, \vec{x}_2)$ is the two-electron singlet ground-state wave function of target $(Z_T; e_1, e_2)_{1s^2:\,^1S}$. Also $\varphi_{nlm}(\vec{s}_1)$ and $\varphi_{1s}(\vec{x}_2) = \sqrt{Z_T^3/\pi}\, e^{-Z_T x_2}$ are the bound-state wave functions of the hydrogen-like atomic systems $(Z_P, e_1)_{nlm}$ and $(Z_T, e_2)_{1s}$ of binding energies $E_{f_1} = -Z_P^2/(2n^2)$ and $E_{f_2} = -Z_T^2/2$, respectively. According to the remark made in the paragraph preceding Eq. (1), the same result for the transition amplitude T_{if} would be obtained if the second term exc(1, 2) in Eq. (3) is omitted and the remaining expression multiplied by $\sqrt{2}$. This is how we will presently proceed.

In Eq. (2), the product $\mathcal{E}_i^+ \mathcal{E}_f^{-\star}$ in $\Phi_i^+ \chi_f^{-*}$ gives a single $\vec{R}$-dependent term $\mathcal{E}_i^+ \mathcal{E}_f^{-\star} = (\rho v)^{2i\nu_i} (vR + \vec{v}\cdot\vec{R})^{i\xi}$. Here, $\xi = Z_P/v$ and $\vec{\rho}$ is the projection of vector $\vec{R}$ onto the XOY plane ($\vec{\rho} = \vec{R} - \vec{Z}$, $\vec{\rho}\cdot\vec{Z} = 0$). The distortion

$(\rho v)^{2i\nu_i} \equiv (\rho v)^{2iZ_P(Z_T-2)/v}$ is due to the Coulomb repulsion between Z_P and $Z_T - 2$. The multiplying term $(\rho v)^{2i\nu_i}$ does not contribute to the total cross section for any values of Z_P and Z_T [23]. In the special case for a helium target ($Z_T = 2$), the phase factor $(\rho v)^{2iZ_P(Z_T-2)/v}$ reduces to unity. As such, differential cross sections in the BCIS-4B method are proportional to $|T_{if}|^2$ and this obviates a difficult numerical quadrature in the Fourier-Bessel transform with a highly oscillatory integrand [23].

In the eikonal mass limit ($1/M_{P,T} \ll 1$) and at small scattering angles, Eq. (2) reads as

$$T_{if}(\vec{\eta}) = Z_P N^{-*}(\nu_T) \iiint d\vec{s}_1 d\vec{s}_2 d\vec{R} \varphi^*_{nlm}(\vec{s}_1)\varphi^*_{1s}(\vec{s}_2) \times \left(\frac{2}{R} - \frac{1}{s_1} - \frac{1}{s_2}\right)\varphi_i(\vec{x}_1, \vec{x}_2)\, e^{i\vec{k}_i\cdot\vec{r}_i + i\vec{k}_f\cdot\vec{r}_f} \times {}_1F_1(i\nu_T, 1, ivx_1 + i\vec{v}\cdot\vec{x}_1)(vR + \vec{v}\cdot\vec{R})^{i\xi}, \quad (4)$$

$$\vec{k}_i\cdot\vec{r}_i + \vec{k}_f\cdot\vec{r}_f = \vec{\alpha}\cdot\vec{s}_1 + \vec{\beta}\cdot\vec{x}_1 = -\vec{v}\cdot\vec{x}_1 - \vec{\alpha}\cdot\vec{R} = -\vec{v}\cdot\vec{s}_1 + \vec{\beta}\cdot\vec{R}, \quad (5)$$

where $\vec{\alpha} = \vec{\eta} - \alpha_z\hat{\vec{v}}$, $\vec{\beta} = -\vec{\eta} - \beta_z\hat{\vec{v}}$, and $\hat{\vec{v}} = (1/v)\vec{v}$. Further, $\vec{\alpha} + \vec{\beta} = -\vec{v}$, $\alpha_z = v/2 - (1/v)\Delta E$, and $\beta_z = v/2 + (1/v)\Delta E$. Here, $\Delta E = E_i - (E_{f_1} + E_{f_2})$, where E_i is the binding energy of the ground state of a two-electron target. The transverse momentum transfer is denoted by $\vec{\eta} = (\eta\cos\phi_\eta, \eta\sin\phi_\eta, 0)$, where $\vec{\eta}\cdot\vec{v} = 0$. The wave function of the initial ground state of a two-electron target will be taken as $\varphi_i(\vec{x}_1, \vec{x}_2) = \sum_{k_1,k_2}\varphi_{\alpha_{k_1}}(\vec{x}_1)\varphi_{\alpha_{k_2}}(\vec{x}_2)$. Here, $\varphi_{\alpha_s}(\vec{r}) = N_{\alpha_s}\exp(-\alpha_s r)$, $N_{\alpha_s} = a_s\sqrt{N}$ $(s = k_1, k_2)$ and N is the normalization constant. The numbers k_1 and k_2 as well as the variationally determined parameters α_s and a_s depend on the choice of wave function. Using ${}_1F_1(i\nu_T, 1, ivx_1 + i\vec{v}\cdot\vec{x}_1) = \int_0^1 d\tau f(\tau) e^{i(vx_1 + \vec{v}\cdot\vec{x}_1)\tau}/[\Gamma(i\nu_T)\Gamma(1 - i\nu_T)]$, where $f(\tau) = \tau^{i\nu_T - 1}(1-\tau)^{-i\nu_T}$, the transition amplitude T_{if} from Eq. (4) becomes

$$T_{if}(\vec{\eta}) = \mathcal{M}\int_0^1 d\tau f(\tau)\mathcal{P}_{if}(\tau), \quad \mathcal{M} = \frac{N^{-*}(\nu_T)}{\Gamma(i\nu_T)\Gamma(1 - i\nu_T)}, \quad (6)$$

$$\mathcal{P}_{if}(\tau) = \sum_{k_1,k_2} N_{\alpha_{k_1}} N_{\alpha_{k_2}} \int d\vec{R}\, e^{i\vec{\beta}\cdot\vec{R}}(vR + \vec{v}\cdot\vec{R})^{i\xi}\mathcal{K}(\vec{R}), \quad (7)$$

$$\mathcal{K}(\vec{R}) = Z_P \iint d\vec{s}_1\, d\vec{s}_2\, \varphi^*_{nlm}(\vec{s}_1)\varphi^*_{1s}(\vec{s}_2)\, e^{-i\vec{v}\cdot\vec{s}_1} \times \left(\frac{2}{R} - \frac{1}{s_1} - \frac{1}{s_2}\right)e^{-\alpha_{k_2}x_2}\psi_{k_1}(\vec{x}_1) = Z_P\left[\frac{2}{R}W_R^{(k_1,k_2)}(\vec{R}) - W_{s_1}^{(k_1,k_2)}(\vec{R}) - W_{s_2}^{(k_1,k_2)}(\vec{R})\right], \quad (8)$$

$$W_R^{(k_1,k_2)}(\vec{R}) = \mathcal{A}_{k_1}\mathcal{C}_{k_2}, \quad W_{s_1}^{(k_1,k_2)}(\vec{R}) = \mathcal{B}_{k_1}\mathcal{C}_{k_2}, \quad W_{s_2}^{(k_1,k_2)}(\vec{R}) = \mathcal{A}_{k_1}\mathcal{D}_{k_2}, \quad (9)$$

$$\mathcal{A}_{k_1} = \int d\vec{s}_1\varphi^*_{nlm}(\vec{s}_1)\, e^{-i\vec{v}\cdot\vec{s}_1}\psi_{k_1}(\vec{x}_1),$$

$$\mathcal{B}_{k_1} = \int d\vec{s}_1\varphi^*_{nlm}(\vec{s}_1)\,\frac{1}{s_1}e^{-i\vec{v}\cdot\vec{s}_1}\psi_{k_1}(\vec{x}_1), \quad (10)$$

$$\mathcal{C}_{k_2} = \int d\vec{s}_2\,\varphi^*_{1s}(\vec{x}_2)\, e^{-\alpha_{k_2}x_2} = \frac{8\sqrt{\pi}Z_T^{3/2}}{\gamma_{k_2}^3},$$

$$\mathcal{D}_{k_2} = \int d\vec{s}_2\,\frac{1}{s_2}\varphi^*_{1s}(\vec{x}_2)\, e^{-\alpha_{k_2}x_2}, \quad (11)$$

where $\psi_{k_1}(\vec{x}_1) = e^{-\alpha_{k_1}x_1 + i(vx_1 + \vec{v}\cdot\vec{x}_1)\tau}$ and $\gamma_{k_2} = Z_T + \alpha_{k_2}$. With $\varphi_{nlm}(\vec{s}_1)$ for any nlm, the results for integrals $\mathcal{A}_{k_1}$, $\mathcal{B}_{k_1}$, and $\mathcal{D}_{k_2}$ can be collected from Refs. [24,38,42], so that

$$\mathcal{A}_{k_1} = 4\mu_{k_1}\sqrt{\pi}N_f^{Z_P}(-i)^l\sum_{p=0}^{n_r}\frac{C_p}{2^{n_l}(n_l-2)!}\sum_{\lambda_1=|m|}^{l}(-i)^{\lambda_1}\Omega(\lambda_1, v)\int_0^1 dt\,\frac{t^{n_l-2}(1-t)^{\lambda_2+1}}{\Delta^{2n_l-2\lambda_1-1}}e^{-i\vec{Q}_\beta\cdot\vec{R}}B^{(\Delta)}_{\nu_2\lambda_1,-m}(\vec{R}),$$

$$C_p = \frac{(-n_r)_p(n+l+1)_p}{(l+3/2)_p p!}, \quad (12)$$

$$\mathcal{B}_{k_1} = \mu_{k_1}\sqrt{\pi}\frac{N_f^{Z_P}}{Z_P}(-i)^l\sum_{p=0}^{n_r}\frac{C_p}{2^{n_l-2}(n_l-3)!}\sum_{\lambda_1=|m|}^{l}(-i)^{\lambda_1}\Omega(\lambda_1, v)\int_0^1 dt\,\frac{t^{n_l-3}(1-t)^{\lambda_2+1}}{\Delta^{2n_l-2\lambda_1-3}}e^{-i\vec{Q}_\beta\cdot\vec{R}}B^{(\Delta)}_{\nu_1\lambda_1,-m}(\vec{R}),$$

$$n_r = n - l - 1, \quad a_f = \frac{Z_P}{n}, \quad (13)$$

$$\mathcal{D}_{k_2} = \frac{4\sqrt{\pi}Z_T^{3/2}}{\gamma_{k_2}^2}\left[\frac{2}{\gamma_{k_2}R} - \left(1 + \frac{2}{\gamma_{k_2}R}\right)e^{-\gamma_{k_2}R}\right], \; n_l = p + l + 3, \quad (14)$$

$$\Omega(\lambda_1, v) = \frac{(-1)^m}{\sqrt{4\pi}}(\lambda_1|lm)v^{\lambda_2}(1-\tau)^{\lambda_2}, \; N_f^{Z_P} = 16\pi Z_P\left[\frac{a_f^3}{n}\frac{(n+l)!}{n_r!}\right]^{1/2}\frac{l!(4a_f)^l}{(2l+1)!}, \quad (15)$$

$$(\lambda_1|lm) = \left[\frac{(2l+1)}{(2\lambda_1+1)}\frac{(l+m)!}{(\lambda_1+m)!}\frac{(l-m)!}{(\lambda_1-m)!(\lambda_2!)^2}\right]^{1/2}, \lambda_1 + \lambda_2 = l, \mu_{k_1} = \alpha_{k_1} - iv\tau, \quad (16)$$

$$\Delta^2 = v_1^2 t(1-t) + a_f^2 t + \mu_{k_1}^2(1-t), \; \vec{v}_1 = (1-\tau)\vec{v}, \; \vec{Q}_\beta = [(\tau-1)t - \tau]\vec{v}, \quad (17)$$

where $\nu_j = n_j - \lambda_1$ and $n_j = n_l + j - 2\,(j = 1, 2)$. Here, $B^{(\Delta)}_{\nu_j\lambda_1,-m}(\vec{R}) = \hat{k}_{\nu_j-1/2}(R\Delta)\mathcal{Y}_{\lambda_1,-m}(\vec{R}\,)$ is the B function [90], $\hat{k}_{\nu_j-1/2}(R\Delta) = \sqrt{2/\pi}(R\Delta)^{\nu_j-1/2}K_{\nu_j-1/2}(R\Delta)$ is the reduced Bessel function, and $K_{\nu_j-1/2}(R\Delta)$ is the McDonald function [91]. The regular solid harmonic is $\mathcal{Y}_{lm}(\vec{q}\,) = q^l Y_{lm}(\hat{\vec{q}}\,)$, where $Y_{lm}(\hat{\vec{q}}\,)$ is the usual spherical harmonic. Thus, we can write

$$\mathcal{P}_{if}(\tau) = 16\pi Z_P Z_T^{3/2}(-i)^l N_f^{Z_P}\sum_{k_1,k_2} N_{\alpha_{k_1}} N_{\alpha_{k_2}}\mu_{k_1}\gamma_{k_2}^{-3}\sum_{p=0}^{n_r}\frac{C_p}{2^{n_l}(n_l-2)!}\sum_{\lambda_1=|m|}^{l}(-i)^{\lambda_1}\Omega(\lambda_1,\upsilon)\int_0^1 dt\,\frac{t^{n_l-3}(1-t)^{\lambda_2+1}}{\Delta^{2n_l-2\lambda_1-3}}$$
$$\times\left[\frac{2t}{\Delta^2}I_0^{(p,\lambda_1)} - \frac{2(n_l-2)}{Z_P}I_1^{(p,\lambda_1)} + \frac{2t}{\Delta^2}I_{k_2,0}^{(p,\lambda_1)} + \frac{t}{\Delta^2}\gamma_{k_2}I_{k_2,1}^{(p,\lambda_1)}\right], \tag{18}$$

$$I_\delta^{(p,\lambda_1)} = \int d\vec{R}(\upsilon R + \vec{\upsilon}\cdot\vec{R}\,)^{i\xi}e^{-i\vec{Q}\cdot\vec{R}}B^{(\Delta)}_{\nu_{2-\delta}\lambda_1,-m}(\vec{R}\,)R^{\delta-1}, \tag{19}$$

$$I_{k_2,\delta}^{(p,\lambda_1)} = \int d\vec{R}\,(\upsilon R + \vec{\upsilon}\cdot\vec{R}\,)^{i\xi}e^{-i\vec{Q}\cdot\vec{R}}e^{-\gamma_{k_2}R}B^{(\Delta)}_{\nu_2\lambda_1,-m}(\vec{R}\,)R^{\delta-1}\,;\ \delta = 0, 1. \tag{20}$$

The results for $I_\delta^{(p,\lambda_1)}$ and $I_{k_2,\delta}^{(p,\lambda_1)}$ are available from Refs. [24,42,43] in the following forms:

$$I_\delta^{(p,\lambda_1)} = 4\pi(-2i)^{\lambda_1}\frac{(2n_p^\delta)!}{n_p^\delta!}\sum_{p_r=0}^{n_p^\delta}\frac{(-n_p^\delta)_{p_r}}{\left(-2n_p^\delta\right)_{p_r}}\frac{2^{p_r-n_p^\delta}}{p_r!}\Delta^{p_r}\,G^{(\delta,\,\Delta_0)}_{p_r\lambda_1,-m}(\vec{Q}\,), \tag{21}$$

$$I_{k_2,\delta}^{(p,\lambda_1)} = 4\pi(-2i)^{\lambda_1}\frac{(2n_p)!}{n_p!}\sum_{p_r=0}^{n_p}\frac{(-n_p)_{p_r}}{(-2n_p)_{p_r}}\frac{2^{p_r-n_p}}{p_r!}\Delta^{p_r}\,G^{(\delta,\,\Delta_1)}_{p_r\lambda_1,-m}(\vec{Q}\,), \tag{22}$$

$$G^{(\delta,\Delta_\omega)}_{p_r\lambda_1,-m}(\vec{Q}\,) = \sum_{k=0}^{p_\delta}\sum_{l_1=|m|}^{\lambda_1}\Phi^\omega_{kl_1}(\delta)\mathcal{D}_{l_1,-m}(\vec{Q}\cdot\vec{\upsilon}\,);\ \ \omega = 0,\ 1, \tag{23}$$

$$\mathcal{D}_{l_1,-m}(\vec{Q}\cdot\vec{\upsilon}\,) = (l_1|\lambda_1 m)(-i\upsilon)^{l_2}\mathcal{Y}_{l_1,-m}(\vec{Q}\,), \tag{24}$$

$$(l_1|\lambda_1 m) = \left[\frac{(2\lambda_1+1)}{(2l_1+1)}\frac{(\lambda_1+m)!}{(l_1+m)!}\frac{(\lambda_1-m)!}{(l_1-m)!(l_2!)^2}\right]^{1/2}, \tag{25}$$

$$\Phi^\omega_{kl_1}(\delta) = \left(a^\omega_\delta b^\omega_\delta\right){}_3F_2\left(-k_\delta, -\widetilde{k}_\delta, 1-i\gamma_1; k+\lambda_1+1, -p_\delta-\lambda_1; \frac{1}{A_\omega}\right), \tag{26}$$

$$a^\omega_\delta = \Gamma(1+i\xi)(\lambda_1+1)_{p_\delta}\frac{(2D_\omega)^{p_\delta}}{(\Delta_\omega^2+Q^2)^{\lambda_1}}\mathcal{F}_\omega,\ \ \mathcal{F}_\omega = \frac{B_\omega^{i\xi}}{\Delta_\omega^2+Q^2}, \tag{27}$$

$$b^\omega_\delta = \frac{(1+i\xi)_{l_1}(-i\xi)_{l_2}}{(B_\omega)^{l_2}}\frac{(-p_\delta)_k(i\zeta_2)_k}{(\lambda_1+1)_k}\frac{(-1)^k(C_\omega)^k}{k!}, \tag{28}$$

$${}_3F_2\left(-k_\delta, -\widetilde{k}_\delta, 1-i\gamma_1; k_\lambda, -p_\delta-\lambda_1; \frac{1}{A_\omega}\right) = \sum_{u=0}^{[k_\delta]}\frac{(-k_\delta)_u(-\widetilde{k}_\delta)_u(1-i\gamma_1)_u}{(k_\lambda)_u(-p_\delta-\lambda_1)_u u!}\left(\frac{1}{A_\omega}\right)^u, \tag{29}$$

$$A_\omega = \frac{\Delta_\omega^2}{\Delta_\omega^2+Q^2},\ \ B_\omega = \frac{2(\upsilon\Delta_\omega - i\vec{Q}\cdot\vec{\upsilon}\,)}{\Delta_\omega^2+Q^2},\ \ C_\omega = \frac{\upsilon}{B_\omega\Delta_\omega} - 1,\ \ D_\omega = \frac{A_\omega}{\Delta_\omega}, \tag{30}$$

where $\Delta_0 \equiv \Delta$, $\Delta_1 = \Delta_0 + \gamma_{k_2}$, $n_p = n - \lambda_1 - 1$, $p_\delta = p_r + \delta$, $n_p^\delta = n_p - \delta, k_\delta = (p_\delta - k)/2$, $\widetilde{k}_\delta = k_\delta - 1/2$, $\lambda_1 = l_1 + l_2$, $\gamma_1 = -\xi + il_1$, $k_\lambda = k + \lambda_1 + 1$, $\zeta_2 = -\xi - il_2$, $(\alpha)_k$ is the Pochhammer symbol $(\alpha)_k = \alpha(\alpha+1)(\alpha+2)\cdots(\alpha+k-1)$ with $(\alpha)_0 = 1$, ${}_3F_2$ is the Clausen generalized hypergeometric polynomial [92], and the notation $[k_\delta/2]$ signifies the largest integer contained in the fraction $k_\delta/2$.

The expounded outlines complete the analytical calculation of seven out of nine integrals in T_{if} which is thus reduced to a two-dimensional numerical quadrature

$$T_{if}(\vec{\eta}\,) = \mathcal{N}\sum_{k_1,k_2}\frac{N_{\alpha_{k_1}}N_{\alpha_{k_2}}}{\gamma_{k_2}^3}\int_0^1 d\tau\, f(\tau)\mu_{k_1}\sum_{p=0}^{n_r}\sum_{\lambda_1=|m|}^{l}(-2)^{\lambda_1}C_p\Omega(\lambda_1,\upsilon)\left[X_0^{(\lambda_1,p_r)} - X_1^{(\lambda_1,p_r)}\right],\ \ \mathcal{N} = 16\pi^2 Z_P Z_T^{3/2}(-i)^l\frac{e^{\pi\nu_T/2}}{\Gamma(i\nu_T)}, \tag{31}$$

$$X_{\delta}^{(\lambda_1,p_r)} = \frac{(2n_p^{\delta})!N_f^{Z_P}}{2^{n_l-2-\delta}Z_P^{\delta}(n_l-2-\delta)!n_p^{\delta}!}\sum_{p_r=0}^{n_p^{\delta}}\frac{(-n_p^{\delta})_{p_r}}{(-2n_p^{\delta})_{p_r}}\frac{2^{p_r-n_p^{\delta}}}{p_r!}\int_0^1 dt\,\frac{t^{n_l-\delta-2}(1-t)^{\lambda_2+1}}{\Delta^{2(n_l-\lambda_1-\delta)-p_r-1}}$$
$$\times\left\{\left[2G^{(0,\Delta_0)}_{p_r\lambda_1,-m}(\vec{Q})+2G^{(0,\Delta_1)}_{p_r\lambda_1,-m}(\vec{Q})+\gamma_{k_2}G^{(1,\Delta_1)}_{p_r\lambda_1,-m}(\vec{Q})\right]^{1-\delta}+\left[G^{(1,\Delta_0)}_{p_r\lambda_1,-m}(\vec{Q})\right]^{\delta}\right\}. \quad (32)$$

The differential cross sections (in the center of mass system) and total cross sections are defined by

$$\frac{dQ_{if}}{d\Omega}\left(\frac{a_0^2}{\mathrm{sr}}\right)=\frac{\mu^2}{4\pi^2}|T_{if}(\vec{\eta})|^2,\ Q_{if}(\pi a_0^2)=\frac{1}{2\pi^2 v^2}\int_0^{\infty}d\eta\eta|T_{if}(\vec{\eta})|^2, \quad (33)$$

where $\mu = M_P M_T/(M_P+M_T)$ is the reduced mass of the projectile and target nuclei and "sr" stands for steradians. In Q_{if}, the integral over angle ϕ_η from $\vec{\eta}$ is equal to 2π since T_{if} does not depend on ϕ_η. The integrals over the real variables t and τ are carried out numerically with the Gauss-Legendre quadratures. For integration over τ, the Cauchy regularization of function $f(\tau)$ is employed [25,38]. As in Ref. [93], the remaining integration over η can also be performed by the Gauss-Legendre quadrature after a variable change such as $\eta=(1+x)\sqrt{2/(1-x^2)}$, where $x\in[-1,+1]$. This scales the integration points in Q_{if} toward the dominant forward cone. Alternatively, one can use the Gauss-Laguerre quadrature over η with a scaling $\eta'=\eta/\gamma$, where parameter γ (which varies for different impact energies E) is chosen to preponderantly concentrate the integration grid within the forward direction.

III. RESULTS

The outlines for process (1) will now be applied to one-electron capture by protons from helium targets:

$$\mathrm{H}^+ + \mathrm{He}(1s^2:\ ^1S) \longrightarrow \mathrm{H}(nlm) + \mathrm{He}^+(1s), \quad (34)$$

$$\mathrm{H}^+ + \mathrm{He}(1s^2:\ ^1S) \longrightarrow \mathrm{H}(nl) + \mathrm{He}^+(1s), \quad (35)$$

$$\mathrm{H}^+ + \mathrm{He}(1s^2:\ ^1S) \longrightarrow \mathrm{H}(n) + \mathrm{He}^+(1s), \quad (36)$$

$$\mathrm{H}^+ + \mathrm{He}(1s^2:\ ^1S) \longrightarrow \mathrm{H}(\Sigma) + \mathrm{He}^+(1s). \quad (37)$$

The presently computed cross sections, using the two-electron correlated and uncorrelated wave functions of $\mathrm{He}(1s^2:\ ^1S)$ from Refs. [51,52] will be referred to as the "BCIS-4B (Silv)" and "BCIS-4B (Hyll)" methods, respectively. The correlated wave function from Ref. [51] is an open-shell $(1s1s')$ two-parameter wave function, $\varphi_i(\vec{x}_1,\vec{x}_2)=N(e^{-\alpha_1 x_1-\alpha_2 x_2}+e^{-\alpha_2 x_1-\alpha_1 x_2})$ with the binding energy $E_i=-2.8756614$ and the normalization constant $N=[(\alpha_1\alpha_2)^{-3}+(\alpha_1/2+\alpha_2/2)^{-6}]^{-1/2}/(\pi\sqrt{2})$, where $\alpha_1=2.183171$ and $\alpha_2=1.18853$. The uncorrelated wave function from Ref. [52] is a closed-shell $(1s1s)$ one-parameter wave function, $\varphi_i(\vec{x}_1,\vec{x}_2)=(Z_T^{\mathrm{eff}})^3\pi^{-1}e^{-Z_T^{\mathrm{eff}}(x_1+x_2)}$ with the effective target nuclear charge $Z_T^{\mathrm{eff}}=Z_T-5/16=1.6875$ and the binding energy $E_i=-2.84765625$. Both the BCIS-4B (Silv) and BCIS-4B (Hyll) methods are employed for total cross sections. For differential cross sections, only the BCIS-4B (Silv) method is shown. Thus, in Sec. III when dealing with $dQ/d\Omega$, the abridged acronym "BCIS-4B" will mean "BCIS-4B (Silv)."

For more than 70 transitions $1s^2\to nlm$, total and differential cross sections are reported at impact energies $E=$ 10–4000 keV and $E=$ 30–12 500 keV, respectively. State-selective cross sections are denoted by X_{nlm} with $X=Q$ (total) or $X=dQ/d\Omega$ (differential). The cross sections summed over all the pertinent values of m and lm are labeled by X_{nl} and X_n, respectively. The cross section $X_{\Sigma,n_{\max}}$ refers to the sum of X_n $(1\leqslant n\leqslant n_{\max})$ for a fixed maximum value $n_{\max}$ of n. In the cross sections summed over all n, the approximate contributions of the states with $n>n_{\max}$ are included by the Oppenheimer n^{-3} scaling rule [94,95]

$$X_{\Sigma,2}=X_1+1.616X_2,\ X_{\Sigma,3}=X_1+X_2+2.081X_3,$$
$$X_{\Sigma,4}=X_1+X_2+X_3+2.561X_4. \quad (38)$$

The role of the final excited states is known to be lessened with the increased E. We use $n_{\max}=2$, 3, and 4 to arrive at $X_{\Sigma,2}$, $X_{\Sigma,3}$, and $X_{\Sigma,4}$, respectively. The difference between the obtained results for $X_{\Sigma,3}$ and $X_{\Sigma,4}$ is completely negligible, and at higher E, so is the discrepancy between $X_{\Sigma,2}$ and $X_{\Sigma,3}$.

Theoretical state-selective and state-summed cross sections are compared with the experimental data available from different measurements [32,53–89]. As to formation of the target remainder $\mathrm{He}^+(n'l'm')$, only the cross sections for $n'l'm'=1s$ (ground state) are included in our computations. The estimates of the contributions from all the excited $n'l'm'$ states of $\mathrm{He}^+(n'l'm')$ do not exceed 5% according to both theory and measurements [23,96–98]. The quoted measurements for state-resolved and state-summed transitions refer to total cross sections. The measured differential cross sections (angular distributions) in the cited references are for the state-summed transitions alone, i.e., for $(dQ/d\Omega)_\Sigma$.

The total Q (Figs. 1 to 3) and differential $dQ/d\Omega$ (Figs. 4 to 8) cross sections computed at 10 to 4000 and 30 to 12 500 keV, respectively, are accurate to within two decimal places (the tabular data are available from the authors upon request). Cross sections $Q_{\Sigma,n_{\max}}$ at 10 to 4000 keV are for $n_{\max}=4$ and $(dQ/d\Omega)_{\Sigma,n_{\max}}$ at 30 to 12 500 keV are for $n_{\max}=$ 1–4. Whenever it is unnecessary to specify the value of $n_{\max}$, we shall write Q_Σ and $(dQ/d\Omega)_\Sigma$. In the ordinates of Figs. 1 to 8, no subscript will be indicated in Q nor in $dQ/d\Omega$. It will be clear from the context whether Q and $dQ/d\Omega$ refer to the given state-selective or state-summed cross sections.

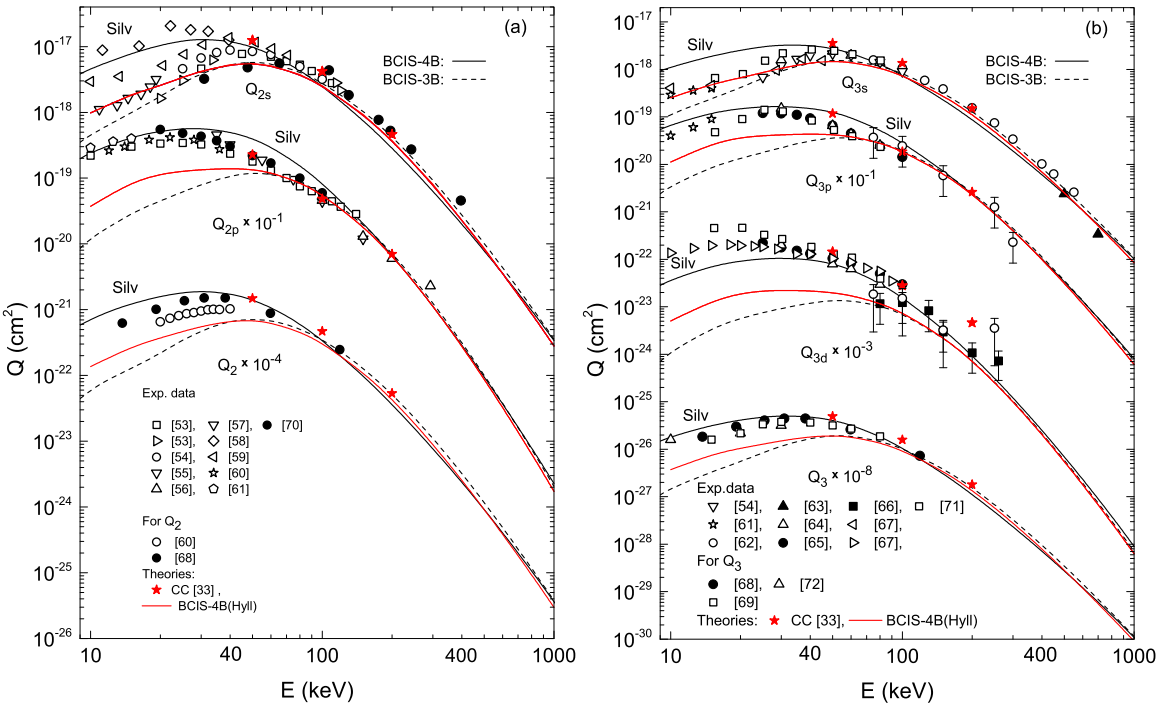

FIG. 1. Formation of H(nl), H($n = 2$), and H($n = 3$) in the $H^+ + He(1s^2)$ collisions (35) and (36).

A. Total cross sections

In Figs. 1 to 3, our total cross sections are $\{Q_{2s}, Q_{2p}, Q_2\}$ [Fig. 1(a)], $\{Q_{3s}, Q_{3p}, Q_{3d}, Q_3\}$ [Fig. 1(b)], $\{Q_{4s}, Q_{4p}, Q_{4d}, Q_{4f}, Q_4\}$ [Fig. 2(a)], Q_5 [Fig. 2(b)], Q_6 [Fig. 3(a)], and $Q_{\Sigma,4}$ [Fig. 3(b)]. Therein, the results of the BCIS-4B (Silv) and BCIS-4B (Hyll) methods are given by the full lines drawn in black and red colors, respectively. If both these lines appear on the same plot, the black full lines are labeled by "Silv" to refer to the correlated wave function φ_i of Silverman *et al.* [51]. However, in the legends to the figures, the sole acronym BCIS-4B, without specifying "Silv" or "Hyll," will always imply the BCIS-4B (Silv) method (in accordance with the same convention already stated for $dQ/d\Omega$). The dashed lines in Figs. 1 to 3 are for the BCIS-3B method [42] and the red-filled star-symbols are for the close-coupling (CC) method [33].

The measured state-resolved and state-summed total cross sections, shown in Figs. 1 to 3, exist for Q_{2s}, Q_{2p}, Q_2, Q_{3s}, Q_{3p}, Q_{3d}, Q_3, Q_{4s}, Q_4, Q_5, Q_6, and Q_Σ. Remarkably, most of these measurements, performed during the past 70 years by means of different techniques, are seen in Figs. 1 to 3 to be in reasonable mutual agreement at $E \geqslant 50$ keV, i.e., slightly above the Massey peaks. Around and below 50 keV, down to 10 keV, depending on the particular values of nl in Q_{nl}, the quality of the existing experimental data from different measurements is visibly uneven. In particular, the most pronounced such discrepancies, e.g., within even an order of magnitude at 10 keV, are for Q_{2s} [Fig. 1(a)]. Also above the Massey peak, there are some occasional disagreements among a few measured cross sections [notably for Q_{3d} in Fig. 1(b)].

For Q_{nl}, Q_n and Q_Σ (Figs. 1 to 3), the BCIS-4B (Silv) results are generally in excellent agreement with the corresponding measured cross sections. Both the BCIS-4B (Silv) results and the measured cross sections exhibit the Massey peaks at the similar positions. The observed differences in the locations of the Massey peaks in the BCIS-4B (Silv) and BCIS-4B (Hyll) predictions are due to the usage of different values for the collisional energy defect ΔE, depending on the initial and final binding energies. For $n = 2$, 3, and 4, cross sections Q_{nl} and Q_n are plotted together in Figs. 1 and 2(a) to directly visualize the relative contributions of Q_{nl} to Q_n.

Below about 100 keV (Figs. 1 to 3), the cross sections in the BCIS-4B (Silv) method lie markedly above those in the BCIS-4B (Hyll) method. However, at 100 to 1000 keV, the BCIS-4B (Silv) and BCIS-4B (Hyll) methods are very close to each other as well as to the cross sections in the BCIS-3B method. Further, for Q_{2s}, Q_{2p}, Q_2, Q_{3s}, Q_{3p}, Q_{3d}, Q_3, and Q_Σ at 50-200 keV, the BCIS-4B (Silv) method is in good accord with the CC method [33]. An exception is noted for Q_{3d} at 200 keV where the CC method overestimates (within a factor of 4) the measured cross section [66], which is seen to be perfectly represented by the BCIS-4B (Silv) method.

For spherically symmetric states ($l = 0$) in Figs. 1 and 2(a), the BCIS-4B (Silv) results agree favorably with the measured cross sections starting above or equal to 30, 25, and 40 keV for Q_{2s}, Q_{3s}, and Q_{4s}, respectively. For Q_{2s}, particularly below 30 keV, a large scatter of the existing experimental data from different recordings hampers testings of the depicted theoretical line shapes and calls for new measurements to clarify the situation. However, regarding Q_{3s} and Q_{4s}, various measurements are mutually concordant. This offers a more definitive test of the theoretical predictions. It is observed in Figs. 1(b) and 2(a) that, this time, the BCIS-4B (Hyll) results for Q_{3s} and Q_{4s} are in the lead since they provide perfect agreement with the experimental data at $E \geqslant 10$ keV. There is a physical reason for this interesting switch. One can easily show that

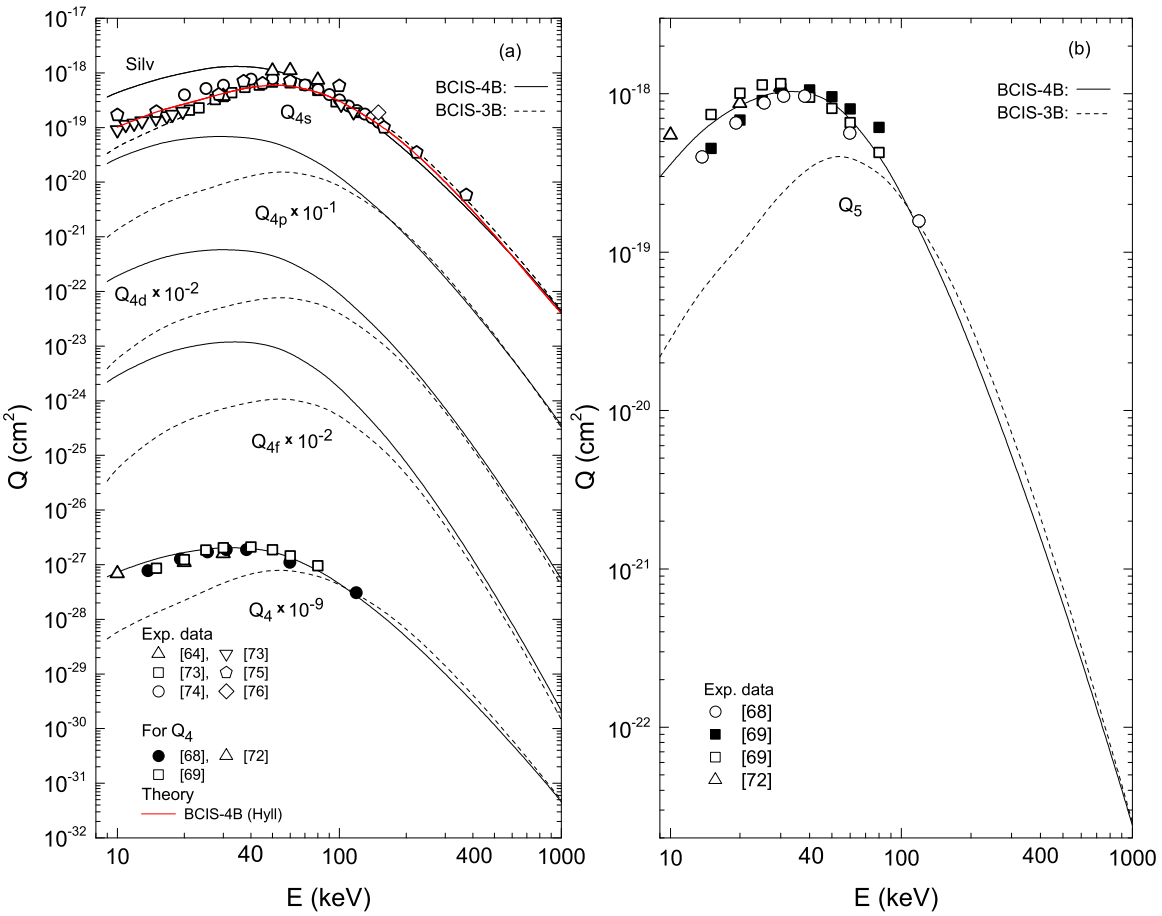

FIG. 2. Formation of H(nl), H($n = 4$), and H($n = 5$) in the $H^+ + He(1s^2)$ collisions (35) and (36).

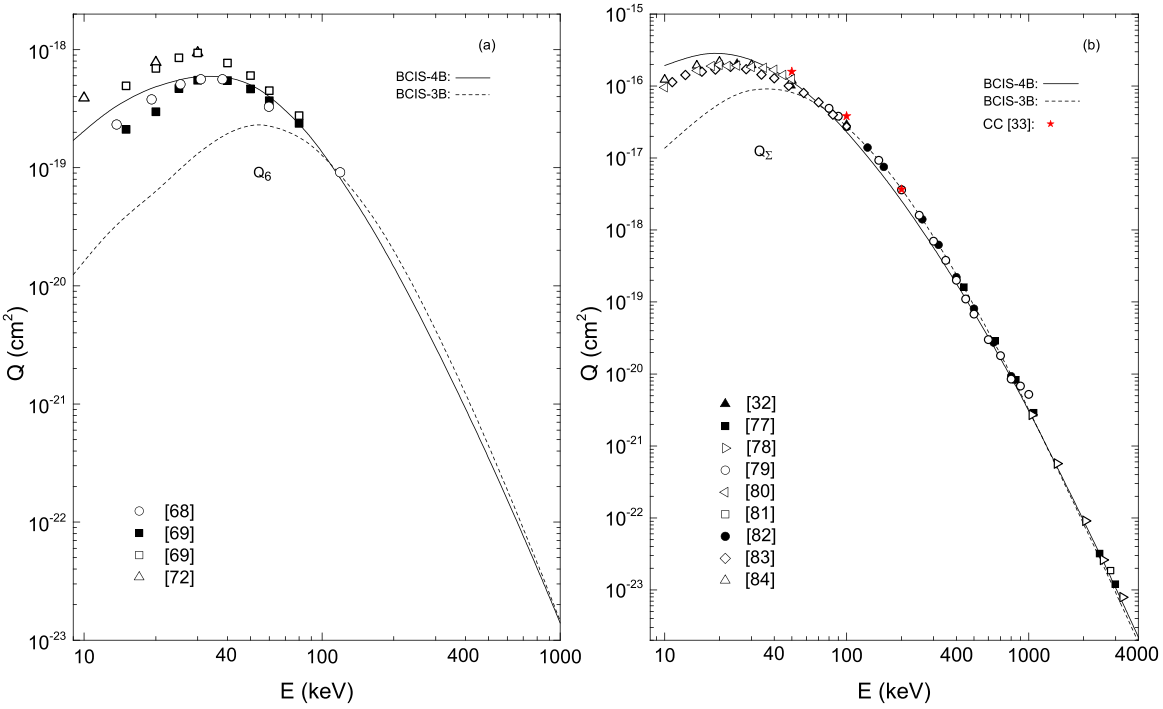

FIG. 3. Formation of H($n = 6$) and H(Σ) in the $H^+ + He(1s^2)$ collisions (36) and (37).

the overlaps of the initial and final bound states in T_{if} for Q_{nl} are better optimized to fit the velocity-matching condition around the Massey peaks with the more appropriate or flexible spatial dependence of the open-shell $(1s1s')$ [51] than with the closed-shell $(1s1s)$ [52] orbitals $\varphi_i(\vec{x}_1, \vec{x}_2)$ for every $l > 0$, while the converse is true for the single case $l = 0$.

In the case of the spherically asymmetric states ($l > 0$), the BCIS-4B (Silv) results faithfully reproduce the experimental data at $E \geqslant 10$, 15, and 30 keV for Q_{2p}, Q_{3p}, and Q_{3d}, respectively. Further, in Figs. 1(a) and 1(b), the BCIS-4B (Silv) results also accurately represent the measured cross sections summed over the lm states, i.e., Q_2 and Q_3, respectively. Herein, the lowest validity limits of the BCIS-4B (Silv) findings for Q_2 and Q_3 are shifted to even smaller energies E than those for Q_{2s} and Q_{3s}, respectively. This is explained by the fact that, around the Massey peaks, cross sections Q_n are appreciably affected by the significant contributions from Q_{nl} with $l > 0$, i.e., from Q_{2p} in Q_2 [Fig. 1(a)] as well as from Q_{3p} and Q_{3d} in Q_3 [Fig. 1(b)].

For $n = 4$, the experimental data for processes (35) and (36) exist only for Q_{4s} and Q_4 [Fig. 2(a)] but, for completeness, all the theoretical cross sections Q_{4l} $(0 \leqslant l \leqslant 3)$ are plotted. As mentioned, the BCIS-4B (Silv) results are almost coincident with the measurements on Q_{4s} at $E \geqslant 40$ keV. Further, beginning already with $E = 10$ keV, a nearly ideal agreement is recorded in Fig. 2(a) between the BCIS-4B (Silv) results and the measured cross sections Q_4. Hence, also for Q_4, the BCIS-4B (Silv) predictions extend their applicability domain to energies E lower than those for Q_{4s}. Here too, as per Fig. 2(a), the explanation is in the considerable contributions from the pertinent subshell cross sections Q_{4p}, Q_{4d} and Q_{4f} to Q_4.

For the higher levels ($n > 4$), a few past measurements were carried out on Q_5 [Fig. 2(b)] and Q_6 [Fig. 3(a)]. Mainly the Massey peak regions (10 to 115 keV) were covered by these measurements that are very well reproduced by the BCIS-4B (Silv) method. The BCIS-4B (Silv) method and the measurements are seen Figs. 1 to 3 to closely obey the adiabatic criterion. According to this criterion, the Massey peak positions are shifted to higher E when l is decreased in Q_{nl} for a fixed n and also when n is augmented in Q_n. Among all the nl states $1 \leqslant l \leqslant n-1$ for a fixed n, the energies $E_{\max}$ at the Massey peak locations are the largest for Q_{ns} $(l = 0)$.

As to capture into any state of atomic hydrogen H(Σ), the results for $Q_{\Sigma,4}$ in the BCIS-4B (Silv) method shown in Fig. 3(b) are very harmonious with the associated measurements at 20 to 4000 keV. The same conclusion remains true also above 4000 keV [not shown in Fig. 3(b) to avoid clutter], including 10 500 keV, which is the highest energy at which Q_Σ has been measured [89]. Specifically, at 10 to 10 500 keV, the perfect performance of the BCIS-4B method is found to extend over 11 orders of magnitude of Q_Σ at energies E covering three or more orders of magnitudes. Such an accomplishment is very important for advancing this problem area since the validity of perturbative theories is usually taken for granted to be limited primarily to high energies (above 100 keV/amu). However, as demonstrated here, such a restriction is surmounted by the BCIS-4B (Silv) method.

We also computed the total cross sections $Q_{\Sigma,1}$ at 10 to 12 500 keV in the BCIS-4B (Silv) method with and without the mentioned extra capture channel, i.e., by including and excluding potential $V_{i,P2}$ from perturbation V_i, respectively. The results indicate that the measurements favor the theoretical predictions with the inclusion of $V_{i,P2}$, i.e., with the complete prior interaction V_i. To illustrate this important point, it suffices to give the percentage of the relative deviations of $Q_{\Sigma,1}$ ($V_{i,P2}$ excluded) from $Q_{\Sigma,1}$ ($V_{i,P2}$ included) as 0.41%, 9.03%, 15.42%, 20.77%, 28.83%, 41.68%, and 44.9% at 30, 60, 100, 150, 300, 1300, and 2500 keV, respectively. Hence, in Q, the importance of the extra capture channel by way of $V_{i,P2}$ rises with augmentation of E. This is reminiscent of the well-established increased role of the dynamic $e_1 - e_2$ correlations at higher E when a four-body transition amplitude in its post form is considered [45], which contains the electronic repulsive potential $1/r_{12} = 1/|\vec{s}_1 - \vec{s}_2|$ in the perturbation. In the exit channel, the Taylor expansion of $1/s_2$ shows that $1/s_2 \approx 1/r_{12}$ at $R \to \infty$.

To recapitulate, it appears from the presented analysis that between the BCIS-4B (Silv) and BCIS-3B methods, the first is by far more beneficial to use than the second. Moreover, within a four-body formulation, it is much more advantageous to employ the BCIS-4B (Silv) method than the BCIS-4B (Hyll) method. Crucially, both conclusions are established in the very important energy domain, which surrounds the Massey peak (10 to 100 keV) where, generally, the BCIS-4B (Silv) method very successfully reproduces the measured cross sections.

B. Differential cross sections

In the total cross sections Q, the integrals over scattering angles can smooth out some of the hidden structures. This could be exacerbated when the differential cross section to be integrated vary over several orders of magnitude. Due to large masses of heavy scattering aggregates, such variations regularly occur within merely a couple of milliradians. Therefore, there is every interest to peer into the possible structures of angular distributions of the formed hydrogen atoms. This could offer certain valuable insights into the competing mechanisms for charge exchange, depending on the energy E. Thus, comparing theories with measurements on differential cross sections should represent a more stringent testing ground, which can shed some additional light onto the studied problem.

Theoretical and experimental cross sections $(dQ/d\Omega)_n$ and $(dQ/d\Omega)_\Sigma$ are in Figs. 4 to 8 at 30 to 12 500 keV. Herein, as stated, all our four-body computations are in the BCIS-4B (Silv) method. Thus, we will refer to this theory simply as the BCIS-4B method. In Fig. 8, also graphed are the results in the BCIS-3B method alongside those from the nonperturbative methods based on the expansions in atomic orbitals [32,34,36].

As stated earlier, differential cross sections $(dQ/d\Omega)_{\Sigma,n_{\max}}$ are for $n_{\max} = 1$ (30, 60 keV), $n_{\max} = 4$ (0.1, 0.15, 0.3, 1.3, 2.5 MeV), $n_{\max} = 3$ (5, 7.5 MeV), and $n_{\max} = 2$ (12.5 MeV). In Figs. 4 to 7, the results in the BCIS-4B method are presented for $(dQ/d\Omega)_n$ with $1 \leqslant n \leqslant n_{\max}$ as well as for $(dQ/d\Omega)_{\Sigma,n_{\max}}$. Figures 4 and 5(a) are for three intermediate energies ($E = 100$, 150, 300 keV), while Figs. 5(b), 6, and 7 are for five higher energies ($E =$ 1.3,

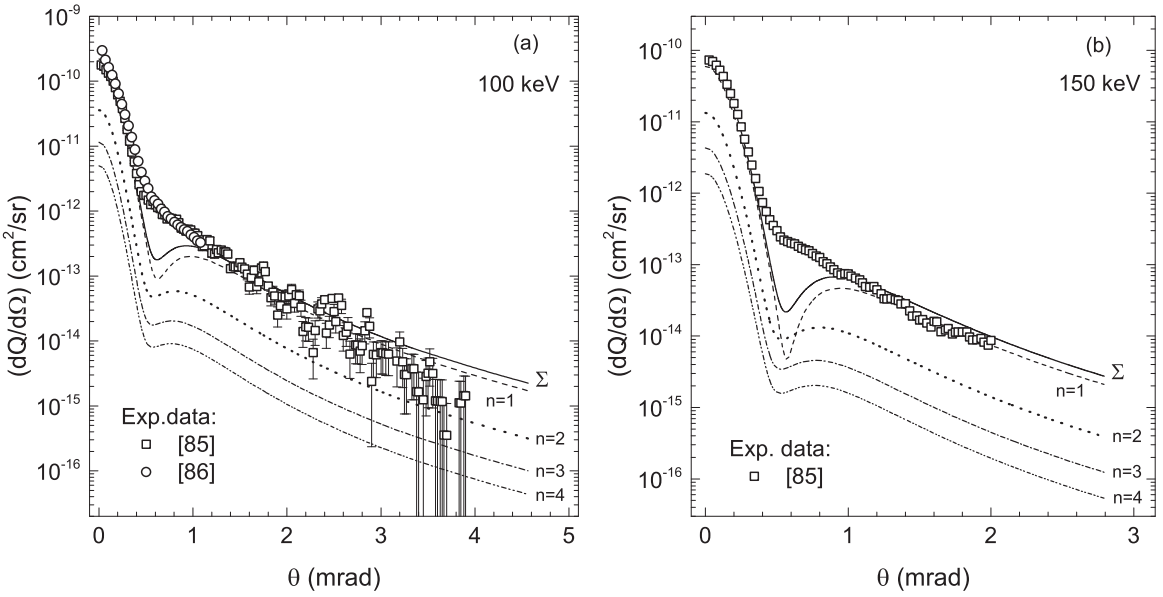

FIG. 4. Formation of H(n) and H(Σ) in the $H^+ + He(1s^2)$ collisions (36) and (37).

2.5, 5.0, 7.5, 12.5 MeV). Finally, Fig. 8 juxtaposes some illustrative theoretical results from the perturbative and nonperturbative methods. All these figures on $dQ/d\Omega$ include also the pertinent experimental data. In Figs. 4 to 8, scattering angles θ and differential cross sections $dQ/d\Omega$ are in the laboratory reference frame.

Generally, the BCIS-4B method is observed to successfully reproduce the measured cross sections at most scattering angles in Figs. 4 to 8. Both theoretical and measured cross sections show certain distinctly characteristic curvature changes at the so-called dark angle $\theta_d \approx 0.5$ mrad (close to the Thomas critical angle $\theta_c = 0.47$ mrad). Of course, energies 100 to 300 keV [Figs. 4, 5(a)] are insufficiently high to enable any clear delineation of the potentially hidden Thomas peaks. However, these are bound to emerge for faster protons, as indeed seen at 1.3 to 12.5 MeV [Figs. 5(b), 6, 7, and 8(d) to 8(f)].

For 100 and 150 keV, around θ_d, unlike the measurements on $(dQ/d\Omega)_\Sigma$, some pronounced minima or dips of $(dQ/d\Omega)_{\Sigma,4}$ appear in the theoretical line shapes, as inherited from each $(dQ/d\Omega)_n$ with $n = 1$–4. However, at 300 keV [Fig. 5(a)], the BCIS-4B method for $(dQ/d\Omega)_n$ with $2 \leqslant n \leqslant 4$ exhibits no minimum or dip. Rather, in these cases, some broadened plateaus occur within 0.4 to 0.8 mrad.

Naturally, for quantitative comparisons between the predicted and measured data, the sum of the computed cross sections $(dQ/d\Omega)_n$ over $n \geqslant 1$ is needed to obtain $(dQ/d\Omega)_{\Sigma,n_{\max}}$. The dominant contributor to $(dQ/d\Omega)_{\Sigma,n_{\max}}$ for any $n_{\max} > 1$ is provided by $(dQ/d\Omega)_1$, which has a minimum or dip within 0.4 to 0.8 mrad [Figs. 4(a) 4(b), and 5(a)]. At 100 to 300 keV, the minima in different cross sections $(dQ/d\Omega)_1$ are only partially compensated by the summed contributions from the excited states $(dQ/d\Omega)_n$ for

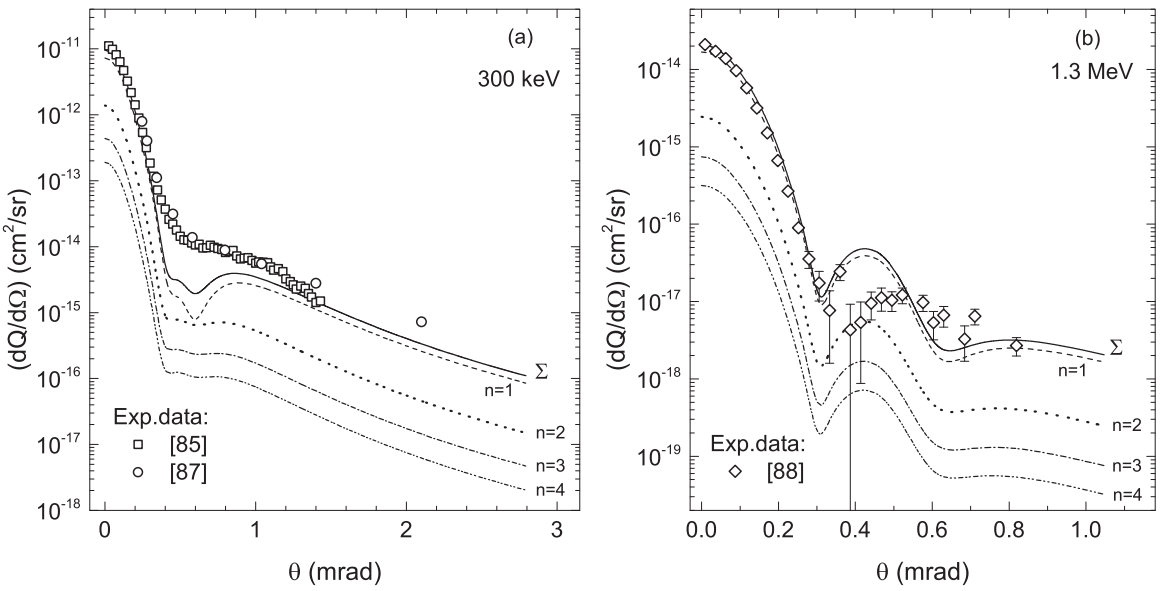

FIG. 5. $H^+ + He \rightarrow H(n, \Sigma) + He^+$.

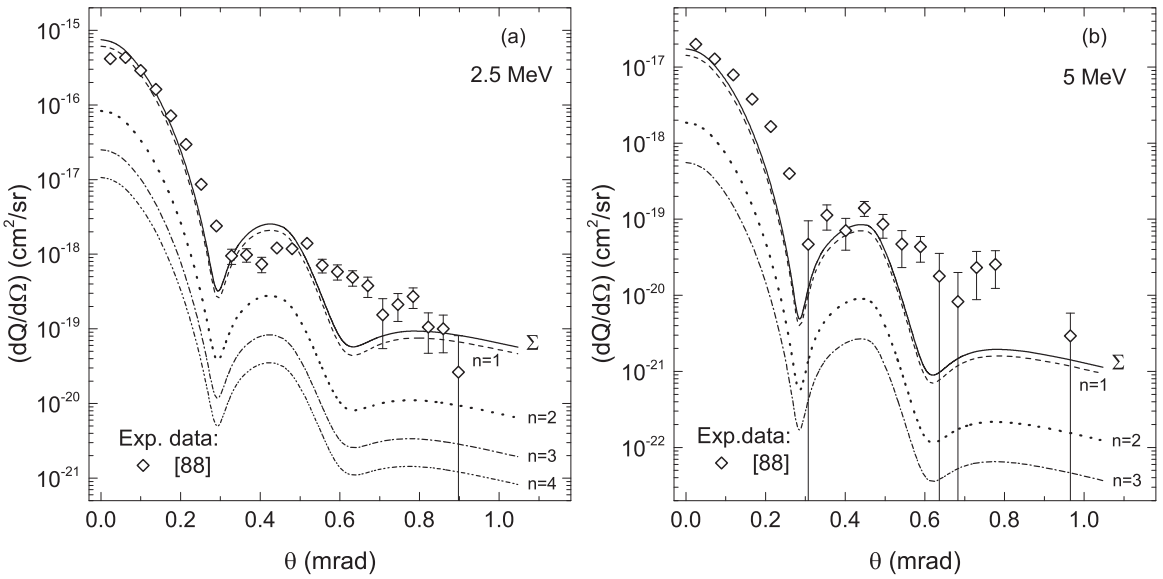

FIG. 6. $H^+ + He \rightarrow H(n, \Sigma) + He^+$.

$n \geqslant 2$. Consequently, the state-summed cross sections such as $(dQ/d\Omega)_{\Sigma,4}$ from the BCIS-4B method in Figs. 4(a), 4(b) and 5(a) also show the minima at 0.4 to 0.8 mrad, where the experimental data depict only the marked slope changes.

The physics of this latter slope change, detected in the experimental data, is understood by the following arguments. Small angle counts of the formed hydrogens recorded in the detectors are due to protons passing far from the helium targets. These large impact parameters correspond to small nuclear deflections, i.e., to negligible Rutherford nucleus-nucleus scatterings. Consequently, the mechanism behind the forward peak is the dominance of proton-electron collisions. Conversely, larger angle counts of atomic hydrogens detected in the measuring devices come from close encounters of the aggregates (small impact parameters) at which the nucleus-nucleus repulsions dominate the projectile-electron attraction. These two mechanisms yield very different line-shapes that are peaked and flattened at smaller and larger angles, respectively. The combining line shape shows a slope change and the inflection point occurs at the intermediate angles, around θ_d, where neither mechanism prevails, as evidenced by the measured differential cross sections shown in Figs. 4(a), 4(b) and 5(a). This reasoning helps clarify the components of a given total cross section, as well. Measured total cross sections Q at a fixed E, as an average of all the recoded counts at each angle, are dominated by the forward cone for heavy scattering aggregates. As such, for ion-atom collisions, the Rutherford internuclear scattering is of no relevance to total cross sections (even down to approximately 0.1 keV/amu).

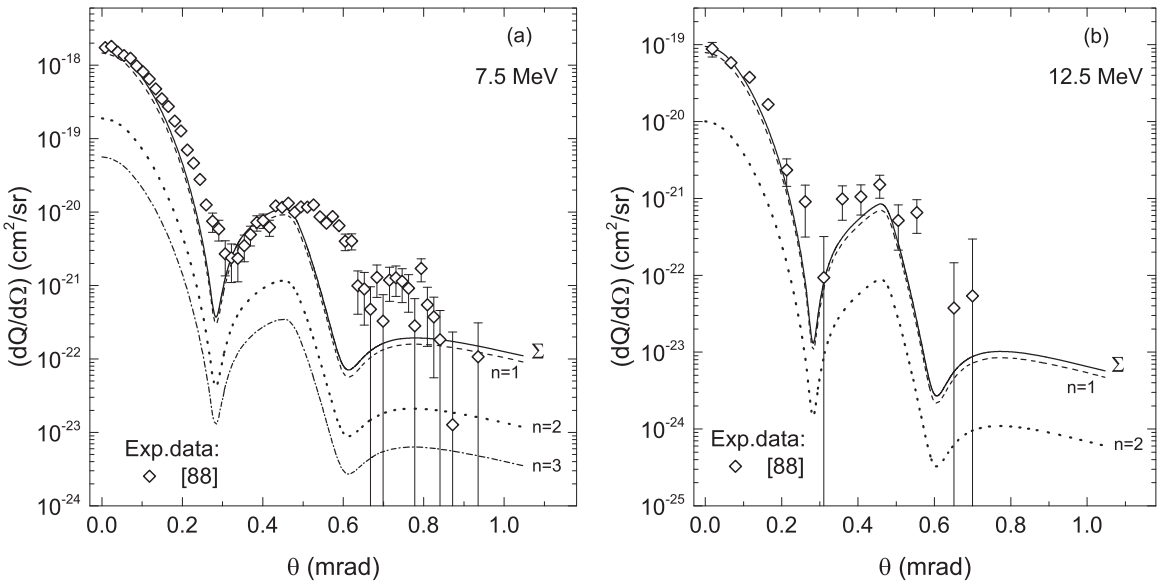

FIG. 7. $H^+ + He \rightarrow H(n, \Sigma) + He^+$.

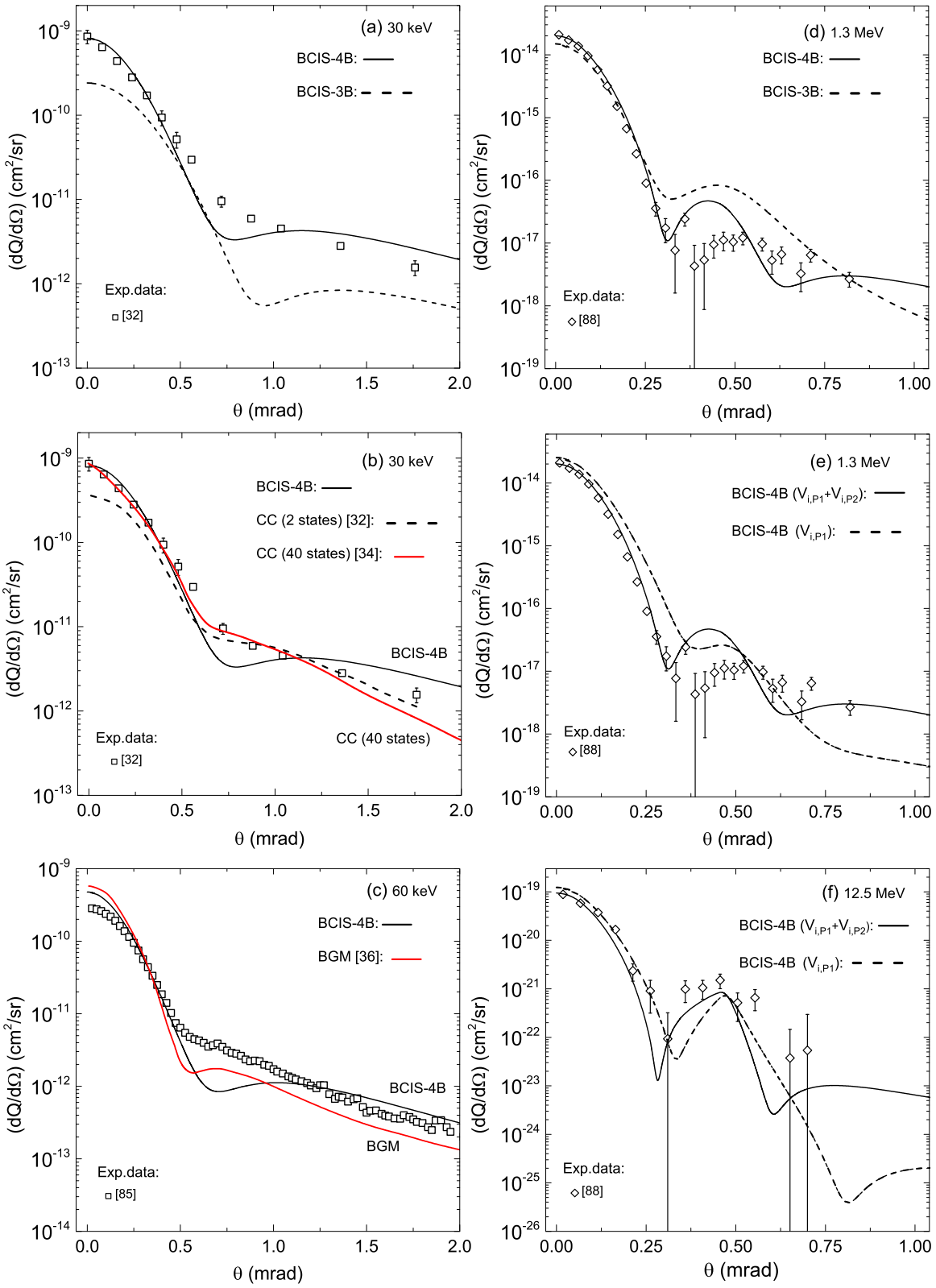

FIG. 8. Formation of H(Σ) in the $H^+ + He(1s^2)$ collision (37).

On the theoretical side, a dip in a differential cross section particularly from the BCIS-4B method, arises from a partial cancellation between the repulsive $2Z_P/R$ and attractive $(-Z_P/s_1 - Z_P/s_2)$ potentials in the perturbation interaction V_i. This cancellation is not complete, i.e., $(dQ/d\Omega)_1 \neq 0$ at θ_d because of a partial compensation by the interference effect between the two highly oscillatory distorting functions (the logarithmic phase for heavy particles and the full Coulomb wave for the electronic motion). A compensation of this type is missing from, e.g., the CB1-4B method which contains

only the heavy particle distortion and consequently leads to an almost true node (zero) of $(dQ/d\Omega)_1$ at θ_d [38]. Even without the presence of the said opposing interactions in potential V_i, minima similar to those in Figs. 4(a), 4(b) and, 5(a) also appear (depending on E) in some other perturbative CDW-type methods [23,29] as well as in the nonperturbative AE-type methods [32,36,37].

The locations of the theoretically predicted minima on Figs. 4(a), 4(b) and 5(a) shift toward the lower scattering angles θ with the increased E. Therein, for the excited states ($n > 1$) at a fixed E, the dips are progressively moved to smaller θ compared with $n = 1$. As a result, a partial filling occurs of the given dip when summing over $(dQ/d\Omega)_n$ in $(dQ/d\Omega)_{\Sigma,n_{\max}}$ for $n_{\max} > 1$. The pattern of the theoretical functions $(dQ/d\Omega)_{\Sigma,4}$ is similar at 100, 150, and 300 keV [Figs. 4(a), 4(b) and 5(a)]. It shows two maxima, separated by a dip, which is subsequently followed by a flatter line-shape tail. The two peaks occur at $\theta = 0$ and around $\theta \approx 0.95$ mrad ($\approx 2\theta_c$). The peak in the forward direction ($\theta = 0$) stems from the projectile-electron interactions (particularly $Z_P - e_1$). The slowly decreasing part of the angular distribution is typical of the Rutherford nucleus-nucleus collisions ($Z_P - Z_T$). In the BCIS-4B method, dominance of the forward peak or the nucleus-nucleus tail is easily identified by switching on or off the two potentials $2Z_P/R$ and $(-Z_P/s_1 - Z_P/s_2)$ in the perturbation interaction V_i from T_{if}.

Specifically, as per theory, our computations confirm that the two competing potentials $2Z_P/R$ and $Z_P(-1/s_1 - 1/s_2)$ in V_i have unequal effects at different scattering angles. Thus, the potential $2Z_P/R$ becomes insignificant when θ approaches the forward scattering region $\theta = 0$, but dominates at larger values of θ. By contrast, $Z_P(-1/s_1 - 1/s_2)$ prevails near $\theta = 0$, but is practically negligible at larger θ. These two mechanisms in the BCIS-4B method yield a slope change in the curves for differential cross sections $(dQ/d\Omega)_{if}$. The location of the slope change is precisely near θ_d, where the contributions from $2Z_P/R$ and $Z_P(-1/s_1 - 1/s_2)$ are of comparable magnitude. This is where the dip appears. After the dip, potential $2Z_P/R$ is the main contributor to V_i and, thus, flattening of the angular distribution points to the pattern of the Rutherford scattering. Independence of the total cross sections Q_{if} of the internuclear potential $V_{PT} = Z_P Z_T/R$ is also readily explained. In the heavy mass limit, transition amplitude T_{if} is influenced by V_{PT} only through a phase, which disappears from Q_{if} upon integrating $|T_{if}|^2$ over scattering angles, or equivalently, over transverse momentum transfers η.

In this slope change of the theoretical curves from Figs. 4(a), 4(b), and 5(a), the passage from the forward peak to the leveled region of the Rutherford scattering goes through a minimum and a maximum. That is how the forward peak at zero angle is accompanied, near 0.95 mrad, by the second peak which is unrelated to the Thomas peak. The position of this second peak also depends on E. It is slightly shifted at, e.g., 150 keV [Fig. 4(b)] with respect to 100 keV [Fig. 4(a)]. As mentioned, there is no dip at 300 keV [Fig. 5(a)] for $Q_{n\geqslant 2}$. However, for $Q_{n=1}$ and Q_Σ, a slight structure appears. Therein, a left bulge near $\theta_c = 0.47$ mrad is an embryo of the Thomas double scattering peak. As noted, while 300 keV is too low for the Thomas peak to become plainly transparent, the conditions for its emergence become more favorable at higher energies. Thus, with increasing E, the genuine Thomas peaks are clearly delineated, as seen is Figs. 5(b) to 7.

As discussed, at sufficiently high E, the critical angle θ_c depends only on the mass ratio m_e/M_P (electron to incident nucleus) and not on E nor on any quantum number. This also applies to the BCIS-4B method, which at 1.3 to 12.5 MeV [Figs. 5(b) to 7] predicts the Thomas peaks at their correct locations for $(dQ/d\Omega)_n$ with $1 \leqslant n \leqslant n_{\max}$ and $(dQ/d\Omega)_{\Sigma,n_{\max}}$. The BCIS-4B method and the measurements show the unsplit Thomas peaks in Figs. 5(b) to 7. In the CDW-3B and CDW-4B methods [22,26,40,41,45,99], the Thomas peaks are often split at $\theta_c \approx 0.47$ mrad due to a destructive interference of the distortions of the unperturbed states in the entrance and exit channels by the initial and final full electronic Coulomb wave functions, respectively [99].

With the augmented E, the width of the Thomas peak is gradually narrowed and the height is concomitantly increased [Figs. 5(b) to 7]. Moreover, comparing the structures at $\theta = 0$ (single scattering) and $\theta_c = 0.47$ mrad (double scattering) in these figures, it is noted that the Thomas peaks become stronger than the forward peaks with the increased E. At still larger energies than those from Figs. 5(b) to 7 (not shown here since there are no experimental data), the Thomas peaks tends to largely overwhelm the forward peaks. This shows the dominance of the second- over the first-order scattering mechanisms at very high energies E.

Between the forward and Thomas maximum, there is a minimum located near $\theta = 0.28$ mrad at each E in Figs. 5(b) to 7. The location of this minimum does not depend on the quantum numbers, i.e., it is the same in $(dQ/d\Omega)_n$ for $1 \leqslant n \leqslant n_{\max}$. Such a minimum is due to a destructive interference between the first- and second-order scattering mechanisms [40,99]. Moreover, Figs. 5(b) to 7 show that the BCIS-4B method gives another two structures after the Thomas critical angle θ_c. Namely, there is a dip at about 0.60 mrad and a very broad peak near 0.80 mrad. Both dips (0.28 and 0.60 mrad) become shallower with augmented energy E. The wide peaks centered at about 0.80 mrad in Figs. 5(b) to 7 merge smoothly into the tails of the Rutherford scattering.

In all the measured differential cross sections [88] [Figs. 5(b) to 7], the larger estimated error bars are around the dips at 0.28 and 0.60 mrad as well as near the peaks at 0.47 and 0.80 mrad. The largest estimated uncertainties of the measurements [88] are for $\theta \geqslant 0.6$ mrad at 2.5 MeV [Fig. 6(a)], 5 MeV [Fig. 6(b)], 7.5 MeV [Fig. 7(a)], and 12.5 MeV [Fig. 7(b)]. After the Thomas peaks, the measurements too seem to indicate some curvature changes within 0.6 to 0.8 mrad. In Figs. 5(b) to 7, there is much scattering among the experimental data points at different angles. This precludes an adequate structure-by-structure comparison of the measured and theoretical data.

Revisiting Figs. 4(a) and 4(b) at 100 and 150 keV, respectively, Fig. 5(a) (300 keV) shows that the dip around 0.55 mrad becomes noticeably wider and shouldered with a bulge marking the onset of the Thomas peak, which eventually develops at higher energies. Below 100 keV, the dips are still present and possess their straight, unstructured forms, according to Figs. 8(a) to 8(c) at 30 and 60 keV. A further insight can be gained by comparing the angular distributions from the BCIS-4B method with those from the other perturbative

[42] and nonperturbative theories [32,34,36]. In Figs. 8(a) to 8(c), both the shapes and magnitudes of differential cross sections change considerably when passing from one method to another. At 30 keV [Fig. 8(a)] and 1300 keV [Fig. 8(d)], the BCIS-4B method compares much more favorably with the measurements than the BCIS-3B method.

In a combined experimental and theoretical study at 25 to 100 keV [32], a pronounced dip around 0.5 mrad in $dQ/d\Omega$ was obtained in the close-coupling two-state atomic expansion (TSAE) method when describing the internuclear interaction V_{PT} by a static potential $V_{PT,S}$. However, the use of the Coulomb interaction $V_{PT,C} = Z_P Z_T/R$ in the TSAE method [32] gives $dQ/d\Omega$, in huge disagreement with the experimental data for 30 keV at all angles θ. This situation was salvaged by employing V_{PT} as a sum of the Coulombic $V_{PT,C}$ and static $V_{PT,S}$ interactions. The resulting $dQ/d\Omega$ was smooth and without any dip, including the area around θ_d [32], as is also seen in our Fig. 8(b). This shows that the angular region of the dip and the curvature change in $dQ/d\Omega$ is extremely sensitive to the choice of different forms of the nucleus-nucleus interaction.

The convergence properties of the close-coupling methods can partially be inferred from Fig. 8(b) by comparing the expansions with two [32] and 40 [34] states. The latter (with $V_{PT,C}$) improves the former (with $V_{PT,S}$) below 0.8 mrad when compared to the experimental data [32]. At energy $E = 60$ keV [Fig. 8(c)], the angular distribution in the BCIS-4B method appears to be similar to that of the basis generator method (BGM) [36]. At the shifted locations as well as with the different depths and breadths, these latter two theories predict the dips within 0.5 to 0.6 mrad, where the experimental data show merely a slope change. Prior to the dips, the two predictions (the present and Ref. [36]) are in good agreement with the measurement [85]. After the dip, toward the Rutherford angular region, the experimental data in Fig. 8(c) lie between the BCIS-4B and BGM line shapes.

Earlier, we noted that electron e_2 exerts a considerable influence on the capture of electron e_1, especially when using a correlated target wave function such as that from Ref. [51]. For the magnitudes of total cross sections Q, this was reflected in their considerable changes within about 45%, especially at higher energies. It is then of interest to see the possible impact of this extra capture channel also on differential cross sections by employing the same helium wave function of Silverman *et al.* [51]. Recall that the supplementary collisional pathway to the capture of electron e_1 contains the Coulomb potential between the nontransferred electron e_2 and Z_P in the combination $V_{i,P2} = Z_P(1/R - 1/s_2)$ which is a part of V_i. This is illustrated at 1.3 MeV [Fig. 8(e)] and 12.5 MeV [Fig. 8(f)] using the BCIS-4B method with and without the said extra channel. At both depicted energies, the extra channel for the capture of e_1 significantly influences the locations and depths of the minima around 0.3 mrad caused by a destructive interference between the single- and double-scattering mechanisms. Also considerably altered by this extra channel is the Rutherford part of the line shapes at both energies. For example, no second minimum around 0.625 mrad is seen at 1.3 MeV by excluding the extra channel. Even at energy as high as 12.5 MeV, the extra channel is prominently active as it displaces the second minimum from 0.6 mrad (full line) to 0.81 mrad (dashed line). Taken together, Figs. 8(e) and 8(f) demonstrate the importance of keeping both channels $V_{i,P1} = Z_P(1/R - 1/s_1)$ and $V_{i,P2}$ in V_i from the transition amplitude T_{if} of the BCIS-4B method.

Summarizing Figs. 5(b) to 7, it can be stated that a very good agreement is observed between the BCIS-4B method and experiments [88]. The main peaks for single scattering (forward) and double scattering (Thomas), observed experimentally, are reproduced well by the present state-summed differential cross sections. As in all the measurements, the Thomas peak is not split in the BCIS-4B method. This is advantageous compared to a sharp splitting appearing often near the center of the Thomas peaks in the CDW-3B and CDW-4B methods [26,40,41,45]. In the BCIS-4B method, after the Thomas peak, there is a dip near 0.6 mrad and a wide peak around 0.8 mrad. This two-fold structure seen in Figs. 8(d) and 8(f) at high energies 1.3 and 12.5 MeV, respectively (hidden in the experimental data [88] within the very large estimated uncertainties) shows up in the present theory also at intermediate energies 100 to 300 keV [Figs. 4(a), 4(b) and 5(a)]. Each computed state-summed differential cross section $(dQ/d\Omega)_{\Sigma,n_{\max}}$ for $1 \leqslant n_{\max} \leqslant 4$ in the BCIS-4B method contains a minima or a dip in a narrow angular region near 0.55 mrad, where the corresponding experimental data exhibit only a slope change.

IV. CONCLUSION

Within the perturbative second-order distorted wave formalism of ion-atom collisions, we examine differential $dQ/d\Omega$ and total Q cross sections for one-electron capture by heavy nuclei from helium-like targets in their ground states ($1s^2$: ^1S). Use is made of the four-body boundary-corrected continuum intermediate state (BCIS-4B) method to cover a very broad range of intermediate and high impact energies E (10 to 12 500 keV). Considered is the passage to the final hydrogen-like state of the captured electron in any quantum numbers nlm (principal n, angular l, magnetic m). Of great practical importance is that seven out of nine integrals in the defining transition amplitude T are calculated analytically. The remaining two integrals are carried out numerically. The obtained comprehensive expressions are applicable to both the uncorrelated and highly correlated two-electron target wave functions φ_i. Importantly, the BCIS-4B method contains an extra channel for capture of the active electron by way of single scatterings of the nontransferred electron with the projectile nucleus. The abundantly exploited three-body methods exclude this channel from the outset.

A general-purpose computer program is written for any nuclear charges of bare ions as projectiles and helium-like atoms as targets. This algorithm is here applied to the prototype $H^+ + He(1s^2) \to H(nlm) + He^+(1s)$ collisions to compute the state-selective and state-summed cross sections (differential, total). Employing the obtained sets $\{(dQ/d\Omega)_{nlm},\ 1 \leqslant n \leqslant 4;\ Q_{nlm},\ 1 \leqslant n \leqslant 6\}$, deduced are the assemblies $\{(dQ/d\Omega)_{nl}, Q_{nl}\}$ (sum over m), $\{(dQ/d\Omega)_n, Q_n\}$ (sum over lm), and $\{(dQ/d\Omega)_\Sigma, Q_\Sigma\}$ (sum over lm and $1 \leqslant n \leqslant n_{\max}$, including $n > n_{\max}$ by means of the Oppenheimer n^{-3} scaling). The predictions by the BCIS-4B method for Q_{nl}, Q_n, Q_Σ, and $(dQ/d\Omega)_\Sigma$ are thoroughly compared with all

the existing experimental data from different measurements performed during the past seven decades.

For the illustrated $H^+ + He(1s^2)$ single charge-exchange process, by primarily focusing on the BCIS-4B method, our goal with Q and $dQ/d\Omega$ is fourfold.

(1) To assess the role of electronic correlations, especially around the Massey peak near 50 keV.

(2) To evaluate the influence of the extra channel for capture of the active electron through proton scattering with the nontransferred electron.

(3) To identify the advantages of the BCIS-4B method relative to the three-body boundary-corrected continuum intermediate state (BCIS-3B).

(4) To determine the lowest energy limits of the validity of the BCIS-4B method for the main examined transitions $He(1s^2) \to H(nl)$, $He(1s^2) \to H(n)$ and $He(1s^2) \to H(\Sigma)$.

The outcomes of the exhaustive analysis of the computed Q and $dQ/d\Omega$, judged by reference to the intrinsic features of the BCIS-4B method *and* the pertinent measured cross sections, run as follows.

(1) The static inter-electron correlations in the initial state φ_i of $He(1s^2)$ are crucial at 10 to 100 keV.

(2) The capture probabilities of the active electron induced by the interaction of the impinging proton with the nontransferred electron increase with rising impact energy E.

(3) Overall, the BCIS-4B method largely outperforms the BCIS-3B method.

(4) The BCIS-4B method with the correlated wave function φ_i of $He(1s^2)$ is in overall excellent agreement with the experimental data from the smaller intermediate energies (around 10 to 40 keV, depending on the final state of the formed atomic hydrogen) to the highest energy (12 500 keV) considered in the measurements.

As to $(dQ/d\Omega)_\Sigma$ at high energies (1.3, 2.5, 5.0, 7.5, 12.5 MeV), the BCIS-4B method gives three main structures consisting of two sharp peaks at $\theta = 0$ and $\theta = 0.47$ mrad attributed to single and double scatterings, respectively. Between these latter two peaks, at $\theta = 0.28$ mrad, lies a *physical* minimum or a dip of a pronounced depth due to the interference of single and double scatterings of the active electron. All three signatures are also detected in the experimental data and these fare well with the BCIS-4B method for the correlated φ_i. Additionally, the BCIS-4B method provides a third peak of a notably lower intensity near $\theta \approx 0.80$ mrad. The third peak is preceded by a dip at $\theta \approx 0.60$ mrad. This third peak was also observed in the measurements (7.4 MeV [81], 7.5 MeV [88]). It should be noted that both the dip at $\theta \approx 0.60$ mrad and the peak at $\theta \approx 0.80$ mrad are found in the BCIS-4B method at all the presently considered energies (0.03 to 12.5 MeV). In other words, the appearance of the supplementary minimum ($\theta \approx 0.60$ mrad) and maximum ($\theta \approx 0.80$ mrad) in the measurements on $dQ/d\Omega$ [81,88] at high energies is well expected from the BCIS-4B method. Thus far, after the Thomas peak at 0.47 mrad, all the known three-body theories for single charge-exchange in the $H^+ + He(1s^2)$ collisions, including the BCIS-3B method, produced some smooth structureless Rutherford line-shape tails.

All told, it is clear that the BCIS-4B method is systematically reliable in accurate descriptions of the available experimental data on total and differential cross sections for single-electron capture by protons from helium targets at widely changing energies $E = 20$–$12\,500$ keV. This particular problem is of fundamental and practical importance in several interdisciplinary research fields where charge-exchange collisions play a significant role.

Yet there is a need for further progress of the theory in this problem area alongside the current vigorous advances in both the perturbative and nonperturbative theories that passed the test of time through a myriad of robust applications on many colliding systems. Among other possibilities, an investigative path forward would be worthwhile to undertake also in, e.g., two exploratory directions. One is the perturbative gold-standard, the boundary-corrected second Born method, which could help clarify the multiple structures in differential cross sections. The other is a variational-type unification of the leading perturbative methods and the basis-set expansion methods to smoothly cover all impact energies with the still readily manageable computational demands.

ACKNOWLEDGMENTS

N.M., I.M., and D.D. thank the Ministry of Science, Technological Development, and Innovations of the Republic of Serbia for support under Contract No. 451-03-47/2023-01/200124. Dž.B. thanks the Radiumhemmet (via the Karolinska University Hospital) and the County Council of Stockholm (via FoUU).

[1] T. E. Cravens, Science **296**, 1042 (2002).
[2] K. Heng and R. A. Sunyaev, Astronomy & Astrophysics **481**, 117 (2008).
[3] R. C. Isler, Plasma Phys. Control. Fusion **36**, 171 (1994).
[4] D. M. Thomas, Phys. Plasmas **19**, 056118 (2012).
[5] H. Anderson, M. G. von Hellermann, R. Hoekstra, L. D. Horton, A. C. Howman, R. W. T. Konig, R. Martin, R. E. Olson, and H. P. Summers, Plasma Phys. Control. Fusion **42**, 781 (2000).
[6] Y. Ralchenko, I. N. Draganić, J. N. Tan, J. D. Gillaspy, J. M. Pomeroy, J. Reader, U. Feldman, and G. E. Holland, J. Phys. B: At. Mol. Opt. Phys. **41**, 021003 (2008).
[7] R. Hemsworth, H. Decamps, J. Graceffa, B. Schunke, M. Tanaka, M. Dremel, A. Tanga, H. P. L. De Esch, F. Geli, J. Milnes, T. Inoue, D. Marcuzzi, P. Sonato, and P. Zaccaria, Nucl. Fusion **49**, 045006 (2009).
[8] O. Marchuk, Phys. Scr. **89**, 114010 (2014).
[9] Dž. Belkić, J. Math. Chem. **47**, 1366 (2010).
[10] Dž. Belkić, Z. Med. Phys. **31**, 122 (2021).
[11] Dž. Belkić, Adv. Quantum Chem. **84**, 267 (2021).
[12] K. Purkait, S. Samaddar, D. Jana, and M. Purkait, Braz. J. Phys. **51**, 1 (2021).
[13] H. Suit, T. DeLaney, S. Goldberg, H. Paganetti, B. Clasie, L. Gerweck, A. Niemierko, E. Hall, J. Flanz, J. Hallman, and A. Trofimov, Radioth. Oncol. **95**, 3 (2010).
[14] *Theory of Heavy Ion Collision Physics in Hadron Therapy*, edited by Dž. Belkić (Elsevier, New York, 2013).

[15] M. A. Rodríguez-Bernal and J. A. Liendo, in Ref. [14], p. 203.
[16] R. D. Rivarola, M. E. Galassi, P. D. Fainstein, and C. Champion, in Ref. [14], p. 231.
[17] C. Champion, J. Hanssen, and R. D. Rivarola, in Ref. [14], p. 269.
[18] *State-of-the-Art-Reviews on Energetic Ion-Atom and Ion-Molecule Collisions*, edited by Dž. Belkić, I. Bray, and A. Kadyrov (World Scientific, Singapore, 2019).
[19] J. J. Bailey, I. B. Abdurakhmanov, A. S. Kadyrov, and I. Bray, in Ref. [18], p. 227.
[20] S. Guatelli, D. Bolst, Z. Francis, S. Inserti, V. Ivanchenko, and A. B. Rosenfeld, in Ref. [18], p. 255.
[21] Dž. Belkić, in Ref. [18], p. 285.
[22] I. M. Cheshire, Proc. Phys. Soc. **84**, 89 (1964).
[23] Dž. Belkić, R. Gayet, and A. Salin, Phys. Rep. **56**, 279 (1979).
[24] Dž. Belkić and H. S. Taylor, Phys. Rev. A **35**, 1991 (1987).
[25] Dž. Belkić, Phys. Rev. A **47**, 3824 (1993).
[26] Dž. Belkić, I. Mančev, and J. Hanssen, Rev. Mod. Phys. **80**, 249 (2008).
[27] D. S. F. Crothers and L. J. Dubé, Adv. At. Mol. Opt. Phys. **30**, 287 (1993).
[28] L. Gulyás, P. D. Fainstein, and T. Shirai, Phys. Rev. A **65**, 052720 (2002).
[29] P. N. Abufager, P. D. Fainstein, A. E. Martínez, and R. D. Rivarola, J. Phys. B: At. Mol. Opt. Phys. **38**, 11 (2005).
[30] B. H. Bransden and L. T. Sin Fai Lam, Proc. Phys. Soc. **87**, 653 (1966).
[31] R. Shakeshaft, Phys. Rev. A **18**, 1930 (1978).
[32] P. J. Martin, K. Arnett, D. M. Blankenship, T. J. Kvale, J. L. Peacher, E. Redd, V. C. Sutcliffe, J. T. Park, C. D. Lin, and J. H. McGuire, Phys. Rev. A **23**, 2858 (1981).
[33] T. G. Winter, Phys. Rev. A **44**, 4353 (1991).
[34] H. A. Slim, E. L. Heck, B. H. Bransden, and D. R. Flower, J. Phys. B: At. Mol. Opt. Phys. **24**, 2353 (1991).
[35] M. F. Ferreira da Silva and J. M. P. Serrão, J. Phys. B: At. Mol. Opt. Phys. **36**, 2357 (2003).
[36] M. Zapukhlyak and T. Kirchner, Phys. Rev. A **80**, 062705 (2009).
[37] A. S. Kadyrov, I. B. Abdurakhmanov, I. Bray, and A. T. Stelbovics, Phys. Rev. A **80**, 022704 (2009).
[38] I. Mančev, N. Milojević, and Dž. Belkić, Phys. Rev. A **91**, 062705 (2015).
[39] D. Dollard, J. Math. Phys. **5**, 729 (1964).
[40] Dž. Belkić, *Principles of Quantum Scattering Theory* (Institute of Physics, Bristol, England, 2004).
[41] Dž. Belkić, *Quantum Theory of High-Energy Ion-Atom Collisions* (Taylor & Francis, London, 2008).
[42] N. Milojević, I. Mančev, D. Delibašić, and Dž. Belkić, Phys. Rev. A **102**, 012816 (2020).
[43] I. Mančev, N. Milojević, and Dž. Belkić, Phys. Rev. A **86**, 022704 (2012).
[44] I. Mančev, N. Milojević, and Dž. Belkić, Phys. Rev. A **88**, 052706 (2013).
[45] Dž. Belkić, R. Gayet, J. Hanssen, I. Mančev, and A. Nuñez, Phys. Rev. A **56**, 3675 (1997).
[46] N. Milojević, I. Mančev, and Dž. Belkić, Phys. Rev. A **96**, 032709 (2017).
[47] I. Mančev, N. Milojević, and Dž. Belkić, Eur. Phys. J. D **72**, 209 (2018).
[48] I. Mančev, N. Milojević, D. Delibašić, and Dž. Belkić, Phys. Scr. **95**, 065403 (2020).
[49] D. Delibašić, N. Milojević, I. Mančev, and Dž. Belkić, At. Data Nucl. Data Tables **139**, 101417 (2021).
[50] D. Delibašić, N. Milojević, I. Mančev, and Dž. Belkić, Eur. Phys. J. D **75**, 115 (2021).
[51] J. N. Silverman, O. Platas, and F. A. Matsen, J. Chem. Phys. **32**, 1402 (1960).
[52] E. A. Hylleraas, Z. Phys. **54**, 347 (1929).
[53] R. H. Hughes, E. D. Stokes, C. Song-Sik, and T. J. King, Phys. Rev. A **4**, 1453 (1971).
[54] R. Cline, P. J. M. van der Burgt, W. B. Westerveld, and J. S. Risley, Phys. Rev. A **49**, 2613 (1994).
[55] D. H. Crandall and D. H. Jaecks, Phys. Rev. A **4**, 2271 (1971).
[56] R. Hippler, W. Harbich, M. Faust, H. O. Lutz, and L. J. Dubé, J. Phys. B **19**, 1507 (1986).
[57] R. Hippler, W. Harbich, H. Madeheim, H. Kleinpoppen, and H. O. Lutz, Phys. Rev. A **35**, 3139 (1987).
[58] L. Colli, F. Cristofori, G. E. Frigerio, and P. G. Sona, Phys. Lett. **3**, 62 (1962).
[59] V. Dose, Helv. Phys. Acta **39**, 683 (1966).
[60] E. P. Andreev, V. A. Ankudinov, and S. V. Bobashev, Sov. Phys. JETP **23**, 375 (1966).
[61] J. S. Risley, F. J. de Heer, and C. B. Kerkdijk, J. Phys. B **11**, 1759 (1978).
[62] J. C. Ford and E. W. Thomas, Phys. Rev. A **5**, 1694 (1972).
[63] R. J. Conrads, T. W. Nichols, J. C. Ford, and E. W. Thomas, Phys. Rev. A **7**, 1928 (1973).
[64] M. C. Brower and F. M. Pipkin, Phys. Rev. A **39**, 3323 (1989).
[65] R. A. Cline, W. B. Westerveld, and J. S. Risley, Phys. Rev. A **43**, 1611 (1991).
[66] J. L. Edwards and E. W. Thomas, Phys. Rev. A **2**, 2346 (1970).
[67] R. H. Hughes, H. R. Dawson, B. M. Doughty, D. B. Kay, and C. A. Stigers, Phys. Rev. **146**, 53 (1966).
[68] R. N. Il'in, V. A. Oparin, E. S. Solov'ev, and N. V. Fedorenko, Sov. Phys. JETP Lett. **2**, 197 (1965).
[69] J. Lenormand, J. Phys. France **37**, 699 (1976).
[70] R. Hoekstra, H. P. Summers, and F. J. DeHeer, Nucl. Fusion **3**, 63 (1992).
[71] R. H. Hughes, E. C. A. Stigers, B. M. Doughty, and E. D. Stokes, Phys. Rev. A **1**, 1424 (1970).
[72] S. V. Bobashev, V. A. Ankudinov, and E. P. Andreev, Sov. Phys. JETP **21**, 554 (1965).
[73] R. H. Hughes, H. R. Dawson, and B. M. Doughty, Phys. Rev. **164**, 166 (1967).
[74] B. M. Doughty, M. L. Goad, and R. W. Cernosek, Phys. Rev. A **18**, 29 (1978).
[75] M. Rodbro and F. D. Andersen, J. Phys. B **12**, 2883 (1979).
[76] E. W. Thomas, J. L. Edwards, J. C. Ford *et al.*, *Fifth ICPEAC, Abstracts* (MIT Press, Cambridge, MA, 1969), p. 462.
[77] L. M. Welsh, K. H. Berkner, S. N. Kaplan, and R. V. Pyle, Phys. Rev. **158**, 85 (1967).
[78] U. Schryber, Helv. Phys. Acta **40**, 1023 (1967).
[79] J. F. Williams, Phys. Rev. **157**, 97 (1967).
[80] J. F. Williams and D. N. F. Dubnar, Phys. Rev. **149**, 62 (1966).
[81] E. Horsdal-Pedersen, C. L. Cocke, and M. Stockli, Phys. Rev. Lett. **50**, 1910 (1983).
[82] M. B. Shah and H. B. Gilbody, J. Phys. B **18**, 899 (1985).
[83] M. B. Shah, P. McCallion, and H. B. Gilbody, J. Phys. B: At. Mol. Opt. Phys. **22**, 3037 (1989).

[84] M. E. Rudd, R. D. DuBois, L. H. Toburen, C. A. Ratcliffe, and T. V. Goffe, Phys. Rev. A **28**, 3244 (1983).
[85] M. S. Schöffler, J. Titze, L. Ph. H. Schmidt, T. Jahnke, N. Neumann, O. Jagutzki, H. Schmidt-Böcking, R. Dörner, and I. Mančev, Phys. Rev. A **79**, 064701 (2009).
[86] D. L. Guo, X. Ma, S. F. Zhang, X. L. Zhu, W. T. Feng, R. T. Zhang, B. Li, H. P. Liu, S. C. Yan, P. J. Zhang, and Q. Wang, Phys. Rev. A **86**, 052707 (2012).
[87] P. Loftager (private communication) (2002).
[88] D. Fischer, M. Gudmundsson, Z. Berényi, N. Haag, H. A. B. Johansson, D. Misra, P. Reinhed, A. Källberg, A. Simonsson, K. Støchkel, H. Cederquist, and H. T. Schmidt, Phys. Rev. A **81**, 012714 (2010).
[89] K. H. Berkner, S. N. Kaplan, G. A. Paulikas, and R. V. Pule, Phys. Rev. **140**, A729 (1965).
[90] E. Filter and E. O. Steinborn, Phys. Rev. A **18**, 1 (1978).
[91] I. S. Gradshteyn and I. M. Ryzhik, *Tables of Integrals, Series and Products* (Academic, New York, 1980).
[92] P. Appell and J. Kampe de Feriet, *Functions Hypergeometriques et Hyperspheriques* (Gauthier-Villars, Paris, 1926).
[93] Dž. Belkić, Phys. Rev. A **37**, 55 (1988).
[94] J. R. Oppenheimer, Phys. Rev. **31**, 349 (1928).
[95] Dž. Belkić, S. Saini, and H. S. Taylor, Phys. Rev. A **36**, 1601 (1987).
[96] R. A. Mapleton, R. W. Doherty, and P. E. Meehan, Phys. Rev. A **9**, 1013 (1974).
[97] H.-K. Kim, M. S. Schöffler, S. Houamer, O. Chuluunbaatar, J. N. Titze, L. Ph. H. Schmidt, T. Jahnke, H. Schmidt-Böcking, A. Galstyan, Yu. V. Popov, and R. Dörner Phys. Rev. A **85**, 022707 (2012).
[98] M. S. Schöffler, H.-K. Kim, O. Chuluunbaatar, S. Houamer, A. G. Galstyan, J. N. Titze, T. Jahnke, L. Ph. H. Schmidt, H. Schmidt-Böcking, R. Dörner, Yu. V. Popov, and A. A. Bulychev, Phys. Rev. A **89**, 032707 (2014).
[99] R. D. Rivarola and J. E. Miraglia, J. Phys. B **15**, 2221 (1982).